UNIVERSIDAD DE CHILE
FACULTAD DE CIENCIAS FÍSICAS Y MATEMÁTICAS
DEPARTAMENTO DE FÍSICA

RAYLEIGH-PLATEAU INSTABILITY ON POLYMERS: FAST 3-D PRINTING OF MECHANIC METAMATERIALS.

TESIS PARA OPTAR AL GRADO DE MAGÍSTER EN CIENCIAS, MENCIÓN FÍSICA

CONSUELO ALEJANDRA CONTRERAS CORDERO

PROFESOR GUÍA:
CLAUDIO FALCON BEAS

PROFESORA CO-GUÍA:
CAROLINA ESPINOZA OÑATE

MIEMBROS DE LA COMISIÓN:
JUDIT LISONI REYES
JOEL MARTHELOT
VIVIANA MERUANE NARANJO

Este trabajo ha sido parcialmente financiado por:
Fondecyt 1190005
Núcleo Milenio en Metamateriales Mecánicos Suaves e Inteligentes

SANTIAGO DE CHILE
2024

INESTABILIDAD DE RAYLEIGH-PLATEAU EN POLÍMEROS: IMPRESIÓN 3D RÁPIDA DE METAMATERIALES MECÁNICOS.

En los últimos años, el estudio e interés por los metamateriales, es decir, estructuras creadas a partir de materiales comunes cuya organización interna genera comportamientos son inusuales o inexistentes en la naturaleza, ha aumentado significativamente, incluyendo un especial enfoque en sus procesos de diseño, fabricación y caracterización. En esta tesis presentamos una forma de explotar la conocida inestabilidad Rayleigh-Plateau en múltiples hilos de un fluido viscoso insertado en una solución elastomérica viscosa en proceso de reticulación para construir rápidamente metamateriales mecánicos. Los parámetros de control de la inestabilidad de Rayleigh-Plateau en el proceso de impresión son la cuociente entre las viscosidad de los fluidos, tensión superficial, caudal y velocidad de inyección que definen el radio inicial y amplitud del movimiento zig-zag, que se sintonizaron externamente para generar metamateriales mecánicos blandos y accionables. Este método nos permite posicionar inclusiones esféricas de un fluido con tamaño controlado de manera periódica dentro de una matriz elástica y, por ende, dotar al material compuesto de propiedades mecánicas inusuales mediante el control de la microestructura interna, tales como la aparición de bandas de transmisión y reflexión para ondas mecánicas que pueden ser modificadas externamente mediante simples deformaciones de compresión mecánica así como la utilización de deformaciones de cizalle para generar filtros quirales para ondas mecánicas. Los metamateriales construidos constan de las siguientes caracteristicas: el tiempo de construcción es de 15 minutos, rango de tamaño entre 10-30 cm y el tamaño de las inclusiones esfericas esta entre los 1-2 mm de diametro, estas dos últimas caracteristicas junto con la cantida y forma del arreglo de gotas quedan a disposición del usuario, puesto que son completamente modificables, sin alterar las propiedades generales del metamaterial creado.

RAYLEIGH-PLATEAU INSTABILITY ON POLYMERS: FAST 3-D PRINTING OF MECHANIC METAMATERIALS.

In recent years, the study and interest in metamaterials, i.e. structures created from common materials whose internal arrangement generates behaviours that are unusual or non-existent in nature, has increased significantly, including a special focus on their design, fabrication and characterisation processes. In this thesis we present a way to exploit the known Rayleigh-Plateau instability in multiple threads of a viscous fluid embedded in a viscous elastomeric solution undergoing cross-linking to rapidly construct mechanical metamaterials. The Rayleigh-Plateau instability control parameters in the printing process are the ratio between the fluid viscosities, surface tension, flow rate and jetting speed that define the initial radius and amplitude of the zig-zag motion, which were externally tuned to generate soft and actuatable mechanical metamaterials. This method allows us to position spherical inclusions of a fluid with controlled size periodically within an elastic matrix and thereby endow the composite material with unusual mechanical properties by controlling the internal micro structure, such as the appearance of transmission and reflection bands for mechanical waves that can be externally modified by simple mechanical compression deformations as well as the use of shear deformations to generate chiral filters for mechanical waves. The constructed metamaterials consist of the following characteristics: the construction time is 15 minutes, the size range is between 10-30 cm, and the size of the spherical inclusions is between 1-2 mm in diameter. These last two characteristics, together with the quantity and shape of the droplet arrangement, are at the disposal of the user since they are completely modifiable without altering the general properties of the created metamaterial.

Maybe I made a mistake yesterday, but yesterday's me is still me.
I am who I am today, with all my faults.
Tomorrow I might be a tiny bit wiser, and that's me, too.
These faults and mistakes are what I am,
making up the brightest stars in the constellation of my life.
I have come to love myself for who I was, who I am and who I hope to become.
Kim Namjoon (BTS)

Acknowledgments

I have to start these acknowledgments with the two people who have supported me all my life. Without them, I would not be where I am. Alejandra and Pablo, you have been the best guides, companions, and parents I could have had. Thank you very much for the love, support, containment, and understanding you have given me all these years; you gave me all the tools you had and always allowed me to go for more. Thank you for allowing me to follow my dreams and study whatever I wanted without any conditions. I know it is hard for you to understand what exactly I do and will do with my life, but know that I will be very happy doing it, and I know that is all that matters to you. I am very proud to have you as parents. Thank you for your effort and desire always to give us the best. I love you very much.

To my sisters, Gabriela and Isidora, I thank you for accompanying me on this journey. During all this time, you have been my motivation to keep improving and have shown me that you can achieve everything you set your mind to. I thank you for everything you allowed me to learn with you and for all the times you kept me in good spirits through laughter, outings, or conversations.

Consuelo, I am deeply grateful for your friendship over the past three years. Your unwavering support, whether it was helping me with my thesis or simply being there to share a laugh, has been invaluable. Our shared experiences, from surviving adventurous trips to comforting each other during tough times, have only strengthened our bond. I look forward to many more adventures with you, exploring our favorite places worldwide and seeing our favorite bands. I love you very much, and now I have another reason to thank the tannies: they brought you into my life. And they also brought me five other wonderful people who have brought nothing but happiness to my life, Conna, Tiare, Vale, Ceci, and Pacha; thank you so much for being the most welcoming, queer, funny, and non-judgmental group of friends I've ever had. With you, I can be myself and express myself without fear of anything (remember, if one goes down, we all go down), and at the same time, I hope to be that person for you, know all that you mean to me, thank you for the support and company in these years and all those to come, I love you all very much.

To all the other people who helped me get where I am:

To Somos12 for being the best, thanks for all the laughs, parties, and company; pure love and good wishes to you!

To everyone at FalconLab, thank you for everything you taught me, believe me, I learned almost everything I know because of you, your guidance, support, and good vibes; I hope you all have great success in your following projects and we get together again in the future, it was a pleasure working with you <3

To all the beautiful people I have met at this university, thanks for the company, the constant support, the good lunches, and the laughs; I hope to continue seeing you in the future. I wish you the best in your future plans and that you get out of this place quickly.

And a special thanks to BTS and DPR IAN; I know it is almost impossible for them to read this. Thank you. I need to write down everything they helped me with in these last four years. They helped me move forward from dark mental moments, stop blaming myself for things that did not correspond, and learn to love myself. Thank you for sharing your problems and learnings through your art and helping more people. I love you very much; I wish you all the happiness and peace.

The biggest thanks and recognition goes to me, I am the only one who knows all the sweat, tears and effort I put into all this work. I am proud of all that I have learned and grown during this process, I know it will not go well in our next challenges, as Yoongi said "Future is gonna be okay". Well done, I love me very much<3!

Table of Content

Table Index

Figure Index

Chapter 1

Introduction

In the last decades the scientific community has focused their interest into the experimental, theoretical and numerical study of metamaterials and specifically mechanical ones, whose non trivial microscopic structure (unit cell) gives them unusual or exotic macroscopic mechanical properties.[1–3]. The growing interest has pushed scientists to create methods [4] to classify and sort their multiple counter-intuitive properties such as auxeticity (negative Poisson's ratio), strain stiffening, or non-reciprocal responses [5] in the case of mechanical metamaterials.

Due to these unusual properties and possible applications, the study of mechanical metamaterials has become a very interesting research area. In order to test these properties mechanically, it is necessary to build samples systematically and quickly. For that purpose, it has been develop a new way of printing by making use of the Rayleigh-Plateau instability in polymeric suspensions that cross-linked and thus solidify. In order to understand the printing method developed, it is necessary to first understand the behavior of the Rayleigh-Plateau instability, which will be explained in the second chapter of this thesis. In this chapter will introduced the topic of mechanical metamaterials from a historical perspective, with the development of the first mechanical metamaterials and their subsequent characterization. The background found in previous studies, the objectives of the research, the methodology and the organization of the thesis will also be presented.

1.1. Context

A metamaterial its an object whose macroscopic physical properties are unusual or nonexistent in nature, they are structures created from common materials whose internal organization generates these behaviors of interest, this internal organization is defined by a microscopic structure called unit cell, which allows us to study the physical properties of the entire material just by studying its behavior against any interaction or stimulus.

The unit cell, or building block, correspond to the constituting unit of each metamaterial, this cell is reproduce periodically in a given direction in order to form the desired pattern, depending on this pattern the characteristics that the material will obtain. There are several types of metamaterials, the ones of interest for this thesis being those elastic materials with mechanical and acoustic properties.

Taking a look back, to the first metamaterials created, it can be seen that the inspiration for the shape for a unit cell usually came from nature, starting with pretty basic patterns that repeats on different natural structures, one of the most common copied form of unit cell is the honeycomb shape, as it can be seen in the work of Mousanezhad from 2015[6] in Fig. 1.1.a, where he creates auxetic metamaterials starting with a simple honeycomb cell and then continues to show how structural hierarchy affects the response of this metematerial to compression. Thereafter, the unit cell arrangement has developed from a very simple form as can be seen in Singamaneni's work [7], where his building block was a square of certain material with defined height and circular hole in the middle as can be seen on Fig. 1.1.b to a very complex structure as shown earlier on Mousanezhad's research. In all of this examples, the unit cell is characterized by specific parameters from which the response of the material will depend on.

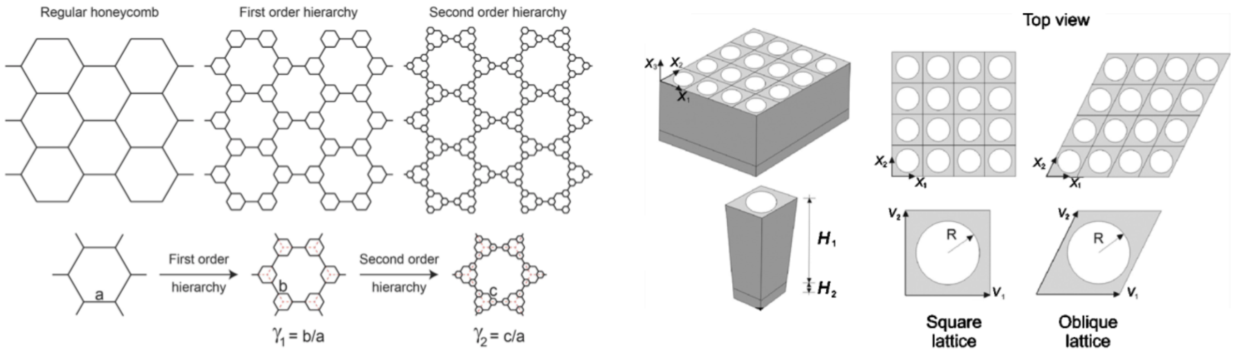

(a) Schematic showing the evolution of a regular hexagonal honeycomb and its corresponding cell into first and second orders of hierarchy.[6]

(b) 4 x 4 periodic representative volume elements (top row) and corresponding primitive cells (bottom row) for square and oblique arrays of cylindrical pores.[7]

Figure 1.1: Types of unit cells

In all this time, there's been different types of metamaterials each and every one with his own construction method. Depending on the primary material used the construction method could signify between hours or days in making one sample for further study. For example, the metamaterials used earlier to describe the various types of unit cells are sheet metal, cast aluminum alloy, vinyl polysiloxane [8, 9], between others. In this thesis, the main material is vinyl polysiloxane (VPS is used from here), so it is important to outline the most common method of constructing elastic mechanical metamaterials using VPS as the main material, as it would help to better understand the importance of the method to be introduced later.

The first step is to design and create a periodic structure with the desired mechanical properties, this is made by studying theoretically and numerically several unit cells and their responses to a certain stimulus; when the design is ready, the next step is to make the technical drawing, in order to have a 3D model of the metamaterial and being able to create the negative structure that is going to be 3D printed. The printing process could take a couple of hours or more depending on the size of the sample that wants to be created. Once the container is finished, the polymer is mixed, poured into the container, waited for it to solidify and then the sample is removed. This whole process described before could take around 10 hours or even more, if the design of the metamaterial or its corresponding building block, its ready, if not the process could take even more time.

As said before, the material of interest correspond to those with acoustically and mechanically responses to propagating waves, therefore the next step is studying the propagation of waves inside the material.

1.2. Background

In all this time, there's been different types of metamaterials each and every one with his own construction method. Depending on the primary material used the construction method could signify between hours or days in making one sample for further study. For example, the metamaterials used earlier to describe the various types of unit cells are sheet metal, cast aluminum alloy, vinyl polysiloxane, between others. In this thesis, the main material is vinyl polysiloxane (VPS is used from here), so it is important to outline the most common method of constructing elastic mechanical metamaterials using VPS as the main material, as it would help to better understand the importance of the method to be introduced later.

The first step is to design and create a periodic structure with the desired mechanical properties, this is made by studying theoretically and numerically several unit cells and their responses to a certain stimulus; when the design is ready, the next step is to make the technical drawing, in order to have a 3D model of the metamaterial and being able to create the negative structure that is going to be 3D printed. The printing process could take a couple of hours or more depending on the size of the sample that wants to be created. Once the container is finished, the polymer is mixed, poured into the container, waited for it to solidify and then the sample is removed. This whole process described before could take around 10 hours or even more, if the design of the metamaterial or its corresponding building block, its ready, if not the process could take even more time.

1.3. Objetives

The overall objective of the thesis is to create mechanical metamaterials in a fast way by occupying the Rayleigh-Plateau instability through the implementation of a 3D printer specially designed for this purpose.

In order to achieve the general objective, theoretical studies of the Rayleigh-Plateau instability and experimental studies of each component linked to the printing process were carried out.

Secondary objectives of this thesis are:

1. To mechanically characterize the band structure of the constructed mechanical metamaterial.
2. To graphically characterize the constructed mechanical metamaterial, establishing the relationship between the parameters of the printing process and the characteristic values of the metamaterial.
3. Theoretically calculate the amplitude of the wave scattered by a spherical inclusion filled with a fluid.

1.4. Methodology

The present thesis is devoted to expose a new method of printing elastic mechanical metamaterials making use of Rayleigh-Plateau instability; in addition to the method, these new metamaterials whose characteristics are presented in the following chapters are also described. In order to create such metamaterials, the experimental configuration described by Tomotika in 1935 will be recreated see Fig. 2.1, where it was established that a thread of viscous fluid within another infinite viscous fluid, destabilized into drops of the same size and separation between them, when interacting with the medium, this study is done in the framework of fluid dynamics, starting from the Navier-Stokes equations for incompressible fluids.

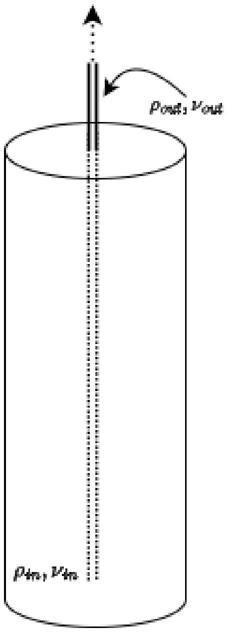

Figure 1.2: Representation of the setup described by Tomotika on this paper[10]

Following the necessary steps, the dispersion relation is obtained as a function of viscosities, densities, thread radius and surface tension between the two fluids, making use of Mathematica to solve the problem numerically and compare with what was obtained by Tomotika, to verify that the presented method will work with the fluids to be chosen. Likewise, a brief review of dispersion theory will be presented, with special emphasis on chiral structures, since this knowledge is necessary to interpret the acoustic measurements that will be obtained. Afterwards, the next step is to design, taking into consideration all the points that the printer must fulfill to work correctly, to then build the printer using additive construction. Then, the code is programmed to control the operation of the printer, defining the parameters that will be used to vary the internal structure of the materials to be created.

Subsequently, the materials obtained by this technique are characterized by computerized tomography in order to see the final internal structure; these images are analyzed in order to know the correlation between size and distance between drops and the initial parameters of the printer. The experimental setup is designed with which the samples will be tested; it is decided to perform acoustic spectroscopy in order to obtain the behavior when varying the internal structure and when rotating the sample on the same axis. Finally, with the results acquire, together with sample's characterization will be analyze to see if the correlation between variables, proposed in the next chapters, was right and explore some applications for the metamaterials created.

1.5. Thesis Organization

The thesis is organized as follows: Chapter 2 contains the theoretical framework of the research, which covers fundamentals of fluid mechanics ,the Navier-Stokes equation, the Rayleigh-Plateau Instability in viscous fluids, to end with the dispersion equation characteristic of our problem. In chapter 3 we will see the dispersion of acoustic waves in elastic media, in order to obtain the possible bands of the metamaterials constructed, the numerical results obtained are shown. Chapter 4 explains in depth the design and creation process of the printer, looking at all the elements that make it up, as well as its electronic operation. In chapter 5, the characterization of the metamaterials constructed is presented, firstly physically through the study of different tomography of the samples and secondly, the acoustic characterization for different configurations of linear and helical periodic patterns.

Chapter 2

Rayleigh-Plateau's Instability

In this chapter it is going to be explained in detail the theory to understand, from the most general concepts, the Rayleigh-Plateau Instability and their dispersion relation, which is important to obtain, as this is going to give us the time range in which the instability it is form.

2.1. Context

The mentioned instability is a naturally produced phenomenon, that converts a stable fluid thread into drops of the same size and separation by the action of capillarity forces. This phenomenon was first observed by Savart, later the phenomenon was described by Plateau [11], who noted that the breakup of the jet happened spontaneously, no matter if there were external forces or not, concluding that the reason behind the drop formation was intrinsic in the fluid dynamics present. And then was Lord Rayleigh [12], who theoretically confirmed the past observations, with this explanation it was possible to obtain the growth rate of the instability.

The only issue or detail, was that Rayleigh in his dynamical theory explained the instability of a long cylindrical fluid thread of an incompressible perfect liquid dominated by capillary forces, not taking in consideration the effect of the fluid that surrounds the thread. Decades later, Tomotika continued with this theory and completed this missing step, adding also into consideration the viscosity of the fluids. The above, can be understood with the explanation of Gallaire and Brun in [13] of the linear instability analysis where explored the possibility of wave number k, frequency ω or both being complex numbers as it shows in the Table 1, defined the instability by the three different behaviors: temporal, spatial or spatio-temporal.

Table 2.1: The three different instability theories explored in Gallaire and Brun review[13]: temporal, spatial and spatio-temporal analysis.

	temporal	**spatial**	**spacio-temporal**
wave number k	$\mathbb{R}$	$\mathbb{C}$	$\mathbb{C}$
frequency ω	$\mathbb{C}$	$\mathbb{R}$	$\mathbb{C}$
condition for instability	$\omega_i > 0$	$-k_i > 0$ and $\frac{dk_r}{d\omega} > 0$	$\omega_i(k_0) > 0$ and $\frac{d\omega_i}{dk_j}(k_0) = \frac{d\omega_i}{dk_r}(k_0) = 0$

The detailed calculation of this theory will be shown below, taking into account that our instability is a temporal type and all the other assumptions necessary to describe the experimental setup to be established in this thesis.

2.2. Fluid Dynamics

2.2.1. General Solution

As said before, we will consider the following configuration: a long cylindrical fluid thread of a viscous incompressible liquid that is surrounded by an infinite mass of another viscous incompressible liquid.

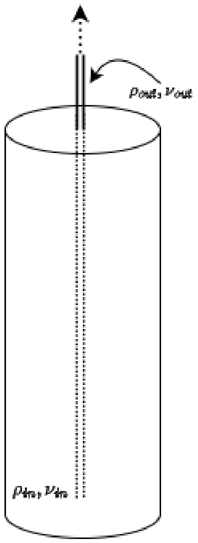

Figure 2.1: Schematic of the theoretical problem with matrix fluid cylinder with density ρ_{in} and ν_{in}, with the injected fluid thread of density ρ_{out} and viscosity ν_{out}.

In order to calculate the dispersion equation of the instability by small perturbations, we have to begin with the equation that governs motion of viscous fluids, Navier-Stokes equation 2.1, along with continuity equation 2.2.

$$\frac{D\vec{V}}{Dt} = -\frac{1}{\rho}\nabla p + \vec{g} + \nu\nabla^2\vec{V} \tag{2.1}$$

$$\nabla \cdot \vec{V} = 0 \tag{2.2}$$

Taking in consideration the configuration described, there is a symmetry along the z axis, therefore only the radial, u, and z component, w, of the velocity is going to matter, transforming 2.1 into the following set of equations:

$$\frac{\partial u}{\partial t} + u\frac{\partial u}{\partial r} + w\frac{\partial u}{\partial z} = -\frac{1}{\rho}\frac{\partial p}{\partial r} + \nu\left(\frac{\partial^2 u}{\partial r^2} + \frac{1}{r}\frac{\partial u}{\partial r} - \frac{u}{r^2} + \frac{\partial^2 u}{\partial z^2}\right) \tag{2.3}$$

$$\frac{\partial w}{\partial t} + u\frac{\partial w}{\partial r} + w\frac{\partial w}{\partial z} = -\frac{1}{\rho}\frac{\partial p}{\partial z} + \nu\left(\frac{\partial^2 w}{\partial r^2} + \frac{1}{r}\frac{\partial w}{\partial r} + \frac{\partial^2 w}{\partial z^2}\right) \tag{2.4}$$

Noting that ν is defined as $\nu = \frac{\mu}{\rho}$, the kinematic coefficient of viscosity and as the fluids are assumed to be incompressible, the equation 2.2 turns into:

$$\frac{\partial u}{\partial r}+\frac{u}{r}+\frac{\partial w}{\partial z}=0 \tag{2.5}$$

Considering the last expression, we take advantage of the axis symmetry present when looking for a function that can satisfy it, since the Strokes current function is a perfect candidate, we can define the velocity components by:

$$u=\frac{1}{r}\frac{\partial \psi}{\partial z},\quad w=\frac{1}{r}\frac{\partial \psi}{\partial r} \tag{2.6}$$

By replacing the new expression for u and w in the set of N-S equations, the term with the pressure can be eliminated, obtaining the following equation when combining both expressions:

$$\left(\frac{\partial}{\partial t}+\frac{1}{r}\frac{\partial \psi}{\partial z}\frac{\partial}{\partial r}-\frac{1}{r}\frac{\partial \psi}{\partial r}\frac{\partial}{\partial z}-\frac{2}{r^2}\frac{\partial \psi}{\partial z}\right)D\psi=\nu DD\psi \tag{2.7}$$

where D is defined as differential operator:

$$D\equiv\frac{\partial^2}{\partial r^2}-\frac{1}{r}\frac{\partial}{\partial r}+\frac{\partial^2}{\partial z^2} \tag{2.8}$$

Looking into the equation 2.7, it can be noted that the general current function ψ can be determine, but, in our case, the solution we are currently looking for is for small perturbations, meaning that all the terms with grade higher than 2 can be neglected and the equation 2.7 reduces to:

$$\left(D-\frac{1}{\nu}\frac{\partial}{\partial t}\right)D\psi=0 \tag{2.9}$$

In order to solve this expression, we can separated the solution in two, ψ_1 and ψ_2, having the first one that solve the first parenthesis and the second one that solves the rest. At this point, its going to be assume that the motions are proportional to e^{int} and e^{ikz}, and the radial part its going to be expressed by a function that only depends on it, obtaining the following type of solutions:

$$\psi_{1,2}=\phi_{1,2}e^{i(nt+kz)} \tag{2.10}$$

Replacing this solutions in 2.9, results in the following set of equations for the radial functions $\phi_{1,2}$:

$$\frac{d^2\phi_1}{dr^2}-\frac{1}{r}\frac{d\phi_1}{dr}-k^2\phi_1=0 \tag{2.11}$$

$$\frac{d^2\phi_2}{dr^2}-\frac{1}{r}\frac{d\phi_2}{dr}-(k^2+\frac{in}{\nu})\phi_2=0 \tag{2.12}$$

If $k_1=k^2+\frac{in}{\nu}$ is defined, both equations would have the same structure,therefore their solutions will do so as well, they would be conform by lineal combination of modified Bessel functions of the 1st order, where A_1,B_1,A_2 and B_2 are proportional constants. Finally the general solution would end up as:

$$\psi=\psi_1+\psi_2=\{[A_1rI_1(kr)+B_1rK_1(kr)]+[A_2rI_1(k_1r)+B_2rK_1(k_1r)]\}e^{i(nt+kz)} \tag{2.13}$$

2.2.2. Specific Solutions

As our case considers the interaction between two viscous fluids, we would have two general solutions, each corresponding to each of the fluids, thus the context of the configuration has to be taken into account and reflected in the solutions.

Given the configuration established, its evident that the components of the velocity, u and w, inside and outside of the thread, has to be finite, this scenario requires that the terms $\frac{\psi}{r}$ and $\frac{1}{r}\frac{\partial\psi}{\partial r}$ must be finite everywhere in both fluids. To fulfill this requirement, we have to look into how the Bessel function are defined in certain regions, for $r = 0$ the $K_1(kr)$ function is not finite, meaning that the solution for the inside liquid can not contain this function, the same goes for the solution of the outside liquid with the function $I_1(kr)$ because is not finite for $r = \infty$, applying this to the solutions we obtain the following current function for the motion inside the column:

$$\psi_{in} = \psi_{in_1} + \psi_{in_2} = \{A_1 r I_1(kr) + A_2 r I_1(k_{in} r)\} e^{i(nt+kz)} \tag{2.14}$$

where

$$k_{in}^2 = k^2 + i\frac{n}{\nu_{in}} \tag{2.15}$$

and $\nu_{in} = \frac{\mu_{in}}{\rho_{in}}$, with μ_{in} is the viscosity and ρ_{in} the density of the inside liquid.

For the liquid mass outside the column, the solution results in:

$$\psi_{out} = \psi_{out_1} + \psi_{out_2} = \{B_1 r K_1(kr) + B_2 r K_1(k_{out} r)\} e^{i(nt+kz)} \tag{2.16}$$

where

$$k_{out}^2 = k^2 + i\frac{n}{\nu_{out}} \tag{2.17}$$

and $\nu_{out} = \frac{\mu_{out}}{\rho_{out}}$, with μ_{out} is the viscosity and ρ_{out} the density of the surrounding liquid.

In order to determine the value of the constants A_1, A_2, B_1 and B_2 presents in equations 2.14 and 2.16, we need to insert physical conditions to the problem, specifically physical conditions at the boundary between the fluids.

2.2.3. Boundary Conditions

The interaction between two viscous fluids has to comply with 3 specific boundary conditions at the interface.

2.2.3.1. 1st Boundary Condition

The first one states that there is not slipping at the surface of the column, this means that the velocity components from both fluids, at the interface, has to be the same, there has to be continuity in the velocity. Mathematically, it can be expressed as follows:

$$(u_{in})_{r=a} = (u_{out})_{r=a}, \quad (w_{in})_{r=a} = (w_{out})_{r=a} \tag{2.18}$$

where a is the radius of the disturbed column. Remembering eq. 2.6, this boundary condition can be expressed in terms of the current function as:

$$\left(\frac{1}{r}\frac{\partial\psi_{in}}{\partial z}\right)_{r=a} = \left(\frac{1}{r}\frac{\partial\psi_{out}}{\partial z}\right)_{r=a}, \quad \left(\frac{1}{r}\frac{\partial\psi_{in}}{\partial r}\right)_{r=a} = \left(\frac{1}{r}\frac{\partial\psi_{out}}{\partial r}\right)_{r=a} \tag{2.19}$$

Substituting the expression for ψ_{in} and ψ_{out} get in 2.14 and 2.16 respectively it is obtain:

$$A_1 I_1(ka) + A_2 I_1(k_{in}a) = B_1 I_1(ka) + B_2 I_1(k_{out}a) \tag{2.20}$$

$$A_1 ka I_0(ka) + A_2 k_{in_1} a I_0(k_{in}a) = -B_1 ka K_0(ka) - B_2 k_{out} a K_0(k_{out}a) \tag{2.21}$$

2.2.3.2. 2nd Boundary Condition

Secondly, we must ensure that tangential stress parallel to the interface is continuous, for if one fluid moves in that direction, the other must also move in the same amount, it cannot stand still or feel a different stress. This can be expressed by the equality of the τ_{zr}-component of the stress tensor when evaluated at the interface:

$$\mu_{in}\left(\frac{\partial^2\psi_{in}}{\partial r^2} - \frac{1}{r}\frac{\partial\psi_{in}}{\partial r} - \frac{\partial^2\psi_{in}}{\partial z^2}\right)_{r=a} = \mu_{out}\left(\frac{\partial^2\psi_{out}}{\partial r^2} - \frac{1}{r}\frac{\partial\psi_{out}}{\partial r} - \frac{\partial^2\psi_{out}}{\partial z^2}\right)_{r=a} \tag{2.22}$$

and again replacing the expression obtain for ψ_{in} and ψ_{out} we get:

$$\begin{aligned}&\mu_{in}\{2A_1k^2 I_1(ka) + A_2(k^2 + k_{in}^2) I_1(k_{in}a)\}\\ &\qquad = \mu_{out}\{2B_1k^2 K_1(ka) + B_2(k^2 + k_{out}^2) K_1(k_{out}a)\}\end{aligned} \tag{2.23}$$

2.2.3.3. 3rd Boundary Condition

For the third boundary condition, we need to remember Young-Laplace equation that states that the pressure difference over an interface between two fluids depends on the surface tension and the principal radii of curvatures of the inner and outer fluid. For the construction of this condition we have to start at the definition for normal stress perpendicular to a surface at a constant radius,

$$p_{rr} = -p + 2\mu\frac{\partial u}{\partial r} \tag{2.24}$$

noting that in our case, the pressure is not constant as is proportional to $e^{i(nt+kz)}$ in the same way as the rest of the motions, we can introduce this and the expression found for the current function into eq. 2.4, in order to obtain an expression for p and replace it in our above equation, by applying some reductions and arrangements, we obtain the following:

$$\frac{p}{\rho} = -\frac{\nu}{ik}\frac{k_1^2 - k^2}{r}\frac{\partial\psi_2}{\partial r} + \frac{n}{k}\frac{1}{r}\frac{\partial(\psi_1 + \psi_2)}{\partial r} \tag{2.25}$$

changing the sub indices to our notation, we obtain the next expression for the normal stress outside the column,

$$p_{rr_{out}} = \mu_{out}\left[\frac{k_{out}^2 - k^2}{ikr}\frac{\partial\psi_{out_2}}{\partial r} + 2ik\frac{\partial}{\partial r}\left(\frac{\partial(\psi_{out_1} + \psi_{out_2})}{r}\right)\right] - \frac{n\rho}{kr}\frac{\partial(\psi_{out_1} + \psi_{out_2})}{\partial r} \tag{2.26}$$

and for inside the column,

$$p_{rr_{in}} = \mu_{in}\left[\frac{k_{in}^2 - k^2}{ikr}\frac{\partial\psi_{in_2}}{\partial r} + 2ik\frac{\partial}{\partial r}\left(\frac{\partial(\psi_{in_1} + \psi_{in_2})}{r}\right)\right] - \frac{n\rho}{kr}\frac{\partial(\psi_{in_1} + \psi_{in_2})}{\partial r} \tag{2.27}$$

Now to obtain the left side of the condition, we need to remember that the Young-Laplace equation is defined as $p = T(\frac{1}{R_1} + \frac{1}{R_2})$, where R_1 and R_2 are the principal radii of curvature and T surface tension, which is supposed constant. Then, we need to find the values of the radii of curvature or the inverse value, the curvature, as is as equally useful, for the z and r direction.

Mathematically, we know that the curvature in the plane of the z-axis is given by $-\frac{\partial^2\zeta}{\partial z^2} = k^2\zeta$, where ζ is the displacement in the r-direction of a particle on the surface of the column and for the perpendicular direction the curvature is $(a+\zeta)^{-1} \approx \frac{1}{a} - \frac{\zeta}{a^2}$, this expression are valid to the outside fluid, because for the inner fluid, we have a long cylinder which principal radii of curvature in the surface are $1/a$ and 0, for the z and r-direction, respectively.

Putting together the Young Laplace equation for the pressure difference between both fluids by replacing what we have until now, we obtain the following expression,

$$p_{rr_{out}} - p_{rr_{in}} \approx T\left(k^2\zeta + \frac{1}{a} - \frac{\zeta}{a^2}\right) - T\left(\frac{1}{a} + 0\right) = \frac{T\zeta}{a^2}(k^2a^2 - 1) \tag{2.28}$$

this indicate that we only need to find a way of expression ζ in terms of currents functions, this is simple since we only need to remember his definition

$$\zeta = \int (u_{in})_{r=a} dt = \int \frac{1}{a}\left(\frac{\partial\psi_{in}}{\partial z}\right)_{r=a} = \frac{k}{na}(\psi_{in})_{r=a} \tag{2.29}$$

And finally replacing in the above equation, we obtain the final expression for the third boundary condition

$$\begin{aligned} &\left[\mu_{out}\{\frac{k_{out}^2 - k^2}{ikr}\frac{\partial\psi_{out_2}}{\partial r} + 2ik\frac{\partial}{\partial r}\left(\frac{\partial(\psi_{out_1} + \psi_{out_2})}{r}\right)\} - \frac{n\rho}{kr}\frac{\partial(\psi_{out_1} + \psi_{out_2})}{\partial r}\right]_{r=a} \\ &\quad = \left[\mu_{in}\{\frac{k_{in}^2 - k^2}{ikr}\frac{\partial\psi_{in_2}}{\partial r} + 2ik\frac{\partial}{\partial r}\left(\frac{\partial(\psi_{in_1} + \psi_{in_2})}{r}\right)\} - \frac{n\rho}{kr}\frac{\partial(\psi_{in_1} + \psi_{in_2})}{\partial r}\right]_{r=a} \\ &\qquad + \frac{Tk(k^2a^2 - 1)}{na^3}[\psi_{in_1} + \psi_{in_2}]_{r=a} \end{aligned} \tag{2.30}$$

However, we can further reduce this formula by replacing the values of $\psi_{in_{1,2}}$, $\psi_{out_{1,2}}$ and grouping according to the constants A_1, A_2, B_1 and B_2,

$$\begin{aligned} &A_1\left\{2i\frac{\mu_{in}}{\mu_{out}}I_1'(ka) - \frac{n\rho_{in}}{\mu_{out}}I_0(ka) + \frac{T(k^2a^2 - 1)}{a^2}\frac{k}{n\mu_{out}}I_1(ka)\right\} \\ &\qquad + A_2\left\{2i\frac{\mu_{in}}{\mu_{out}}kk_{in}I_1'(k_{in}a) + \frac{T(k^2a^2 - 1)}{a^2}\frac{k}{n\mu_{out}}I_1(k_{in}a)\right\} \\ &\qquad\quad - B_1\left\{2ik^2K_1'(ka) + \frac{n\rho_{out}}{\mu_{out}}K_0(ka)\right\} - B_2 2ikk_{out}K_1'(k_{out}a) = 0 \end{aligned} \tag{2.31}$$

where $I_1'(x)$ and $K_1'(x)$ are the first derivatives of $I_1(x)$ and $K_1(x)$ with respect to x, respectively.

2.2.4. Dispersion Equation

From all the calculation done in the previous part, we end up with four equations that will allow us to obtain an expression to know the value of n, or, in other words, to know how long it will take for instability to occur. The equations in question are:

$$\begin{gathered}
A_1 I_1(ka) + A_2 I_1(k_{in}a) - B_1 I_1(ka) - B_2 I_1(k_{out}a) = 0 \\
A_1 ka I_0(ka) + A_2 k_{in_1} a I_0(k_{in}a) + B_1 ka K_0(ka) + B_2 k_{out} a K_0(k_{out}a) = 0 \\
A_1 \frac{2\mu_{in}}{\mu_{out}} k^2 I_1(ka) + A_2 \frac{\mu_{in}}{\mu_{out}} (k^2 + k_{in}^2) I_1(k_{in}a) - B_1 2k^2 K_1(ka) - B_2 (k^2 + k_{out}^2) K_1(k_{out}a) = 0 \\
A_1 F_1 + A_2 F_2 - B_1 F_3 - B_2 F_4 = 0
\end{gathered} \tag{2.32}$$

where

$$\begin{gathered}
F_1 = 2i \frac{\mu_{in}}{\mu_{out}} k^2 I_1'(ka) - \frac{n\rho_{in}}{\mu_{out}} I_0(ka) + \frac{T(k^2a^2 - 1)}{a^2} \frac{k}{n\mu_{out}} I_1(ka) \\
F_2 = 2i \frac{\mu_{in}}{\mu_{out}} k k_{in} I_1'(k_{in}a) + \frac{T(k^2a^2 - 1)}{a^2} \frac{k}{n\mu_{out}} I_1(k_{in}a) \\
F_3 = 2ik^2 K_1'(ka) + \frac{n\rho_{out}}{\mu_{out}} K_0(ka) \\
F_4 = 2ikk_{out} K_1'(k_{out}a)
\end{gathered} \tag{2.33}$$

After some algebraic work, the constants A_1, A_2, B_1 and B_2 can be eliminated and we ended up with the following determinantal equation, that would give us the relationship between n and ka:

$$\begin{vmatrix}
I_1(ka) & I_1(k_{in}a) & K_1(ka) & K_1(k_{out}a) \\
kaI_0(ka) & k_{in}aI_0(k_{in}a) & -kaK_0(ka) & k_{out}aK_0(k_{out}a) \\
\frac{2\mu_{in}}{\mu_{out}} k^2 I_1(ka) & \frac{\mu_{in}}{\mu_{out}} (k^2 + k_{in}^2) I_1(k_{in}a) & 2k^2 K_1(ka) & (k^2 + k_{out}^2) K_1(k_{out}a) \\
F_1 & F_2 & F_3 & F_4
\end{vmatrix} = 0 \tag{2.34}$$

As is possible to solve this equations system, another assumption can be done to simplify a little more our problem, as the aspect that we are considering as most important is the viscosity of the fluids, the effects of the inertia can be neglected by assuming that the densities ρ_{in} and ρ_{out} tends to zero. In order to apply this in our eq. 2.34, is necessary to make an approximation of both densities, because if we replace them by zero in the equation, the first column becomes equal to the third column and the same goes with column 2 and 4, therefore to get a solution the following procedure is needed. First, we assume that ρ_{in} and ρ_{out} are indefinitely small, then expand various functions in column number 2 and 4 in ascending powers of ρ_{in} and ρ_{out}. With this made, several simplifications can be done as dividing all the equation by the product between both densities, to finalize with making $\rho_{in} \to 0$ and $\rho_{out} \to 0$, getting the following equation:

$$\begin{vmatrix} I_1(ka) & kaI_1'(ka) & K_1(ka) & kaK_1'(ka) \\ I_0(ka) & I_0(ka) + kaI_1(ka) & -K_0(ka) & -K_0(ka) + kaK_1(ka) \\ \frac{\mu_{in}}{\mu_{out}} I_1(ka) & \frac{\mu_{in}}{\mu_{out}} kaI_0(ka) & K_1(ka) & -kaK_0(ka) \\ G_1 & G_2 & K_1'(ka) & G_4 \end{vmatrix} = 0 \tag{2.35}$$

where

$$\begin{gathered} G_1 = \frac{\mu_{in}}{\mu_{out}} I_1'(ka) + \frac{T(k^2a^2 - 1)}{2ina\mu_{out}} \frac{1}{ka} I_1(ka), \\ G_2 = \frac{\mu_{in}}{\mu_{out}} (I_1'(ka) + kaI_1''(ka) - I_0(ka)) + \frac{T(k^2a^2 - 1}{2ina\mu_{out}} I_1'(ka), \\ G_4 = K_1'(ka) + kaK_1''(ka) + K_0(ka) \end{gathered} \tag{2.36}$$

Expanding the determinant in eq. 2.35 with respect to fourth row and then solving for in, we found an expression of the following form:

$$n = \frac{T}{2ia\mu_{out}} (1 - k^2a^2) \Phi(ka) \tag{2.37}$$

assuming $x = ka$ then $\Phi(x)$ is a function given by

$$\Phi(x) = \frac{N(x)}{D(x)} \tag{2.38}$$

where

$$\begin{gathered} N(x) \equiv I_1(x) \triangle_1 - (xI_0(x) - I_1(x)) \triangle_2, \\ D(x) \equiv (\frac{\mu_{in}}{\mu_{out}}) \{xI_0(x) - I_1(x)\} \triangle_1 - (\frac{\mu_{in}}{\mu_{out}}) \{(x^2 + 1) I_1(x) - xI_0(x)\} \triangle_2 \\ - \{xK_0(x) - K_i(x)\} \triangle_3 - \{(x^2 + 1) K_1(x) + xK_0(x)\} \triangle_4 \end{gathered} \tag{2.39}$$

and the expression $\triangle_{1,2,3,4}$ are the mini 3×3 determinants that are formed by expanding the expression we are working with

$$\triangle_1 = \begin{vmatrix} xI_0(x) - I_1(x) & K_1(x) & -xK_0(x) - K_1(x) \\ I_0(x) + xI_1(x) & -K_0(x) & -K_0(x) + xK_1(x) \\ (\frac{\mu_{in}}{\mu_{out}}) xI_0(x) & K_1(x) & -xK_0(x) \end{vmatrix},$$

$$\triangle_2 = \begin{vmatrix} I_1(x) & K_1(x) & -xK_0(x) - K_1(x) \\ I_0(x) & -K_0(x) & -K_0(x) + xK_1(x) \\ (\frac{\mu_{in}}{\mu_{out}}) I_1(x) & K_1(x) & -xK_0(x) \end{vmatrix},$$

$$\triangle_3 = \begin{vmatrix} I_1(x) & xI_0(x) - I_1(x) & -xK_0(x) - K_1(x) \\ I_0(x) & I_0(x) + xI_1(x) & -K_0(x) + xK_1(x) \\ (\frac{\mu_{in}}{\mu_{out}}) I_1(x) & (\frac{\mu_{in}}{\mu_{out}}) xI_0(x) & -xK_0(x) \end{vmatrix},$$

$$\triangle_4 = \begin{vmatrix} I_1(x) & xI_0(x) - I_1(x) & K_1(x) \\ I_0(x) & I_0(x) + xI_1(x) & -K_0(x) \\ (\frac{\mu_{in}}{\mu_{out}})I_1(x) & (\frac{\mu_{in}}{\mu_{out}})xI_0(x) & K_1(x) \end{vmatrix}$$

With the above equation, we already find our dispersion equation, which represents the disturbance growth rate, the solution it is going to be found with the help of Mathematica. In Annex A.1 it can be found the notebook made to find the exact solution of this equation, that has the following structure:

$$n = \Phi(x, \mu_{in}, \mu_{out}, T, a) = \frac{T}{2ia\mu_{out}}(1 - k^2a^2)\frac{N(x)}{D(x)} \tag{2.40}$$

2.2.4.1. Parameters Dependence

From Eq.2.40, it is possible to obtain a general idea of how the parameters influence the dispersion relation, specifically in the maximum value of this curve, since it is at this point where the instability is maximum, i.e., for the given parameters, the wavelength that is expressed fastest in the system is the one found by replacing the value of k corresponding to this maximum point.

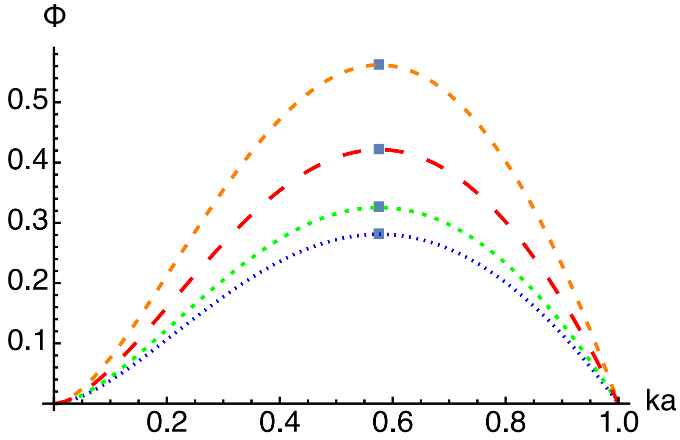

Figure 2.2: Dispersion relation in function of for different values of surface tension T, in order of growth: blue-tiny dashed line (1x), green-small dashed line (1.15x), orange-medium dashed line (1.5x) and red-large dashed line (2x), with T = 19 mN/m and ka_{max} = 0.57606.

In Fig.2.2 it is graph the superficial tension dependence, as seen in the equation for the dispersion relation, this parameter appears as a factor of the quotient between $N(x)$ and $D(x)$, affecting majorly the value of the maximum frequency, i.e, the time in which the instability would develop, concluding that superficial tension between both viscous fluids will not change the wavelength of the resulting thread, it would just affect the time, in this case showed, it just multiply the base time (blue curve) by the factor of each curve.

The next parameter to analyse its effect is the initial radius of the thread, whose behaviour can be seen in Fig.2.3; given the factor $(1 - k^2a^2)$, as the radius gets bigger the shape of the curve gets more flatter, which is added to the effect of the other factor $1/a$, results on a maximum with shorter wavelengths and longer time to develop the instability as the radius increases. The maximum value of ka is 0.57606.

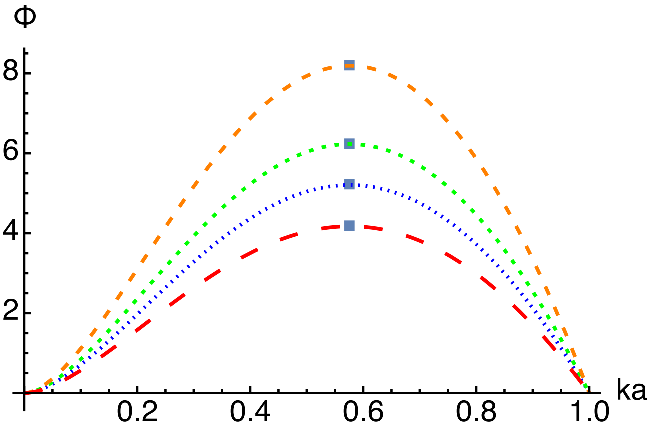

Figure 2.3: Dispersion relation for different values of initial radius, in order of growth: orange-medium dashed line (15 gauge), green-small dashed line (13 gauge), blue-tiny dashed line (12 gauge) and red-large dashed line (10 gauge).

Fig. 2.4 shows the quotient between fluid viscosities. The three first curves have the same matrix fluid (same denominator), but the difference between them is the viscosity of the fluid injected; as this viscosity gets smaller, time lowers too, and wavelength changes, being its high value the case in which the ratio is equal to 0.34 with $ka = 0.5894$. The red and blue curves use the same fluids, differentiating the place they are occupying, giving the possibility to change the wavelength and time of the instability by changing which of the two fluids is being injected and which is the elastic matrix.

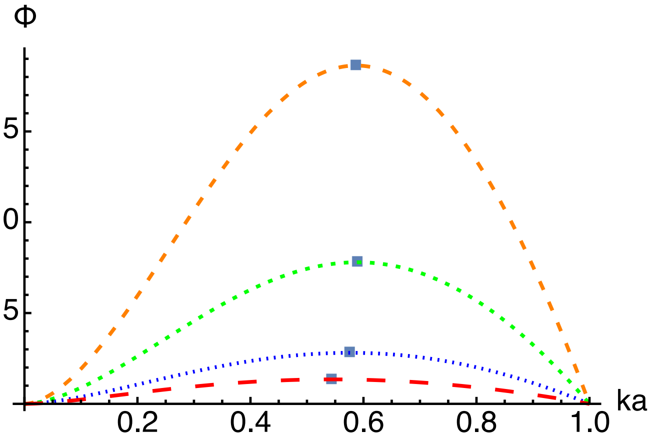

Figure 2.4: Dispersion relation for different values of the viscosity quotient, in order of growth: orange-medium dashed line (0.19), green-small dashed tiny (0.34), blue-tiny dashed line (0.68) and red-large dashed line (1.46).

Chapter 3

Scattering of Acoustic Waves

This chapter aims to introduce the theory of scattering for the configurations of the metamaterial created to have an idea of how the band structure would be. As the development of this theory is still in process and the complexity of it means creating a whole new theoretical thesis, this chapter will be tackled based on the preliminary results obtained. Then, the first part will state the problem of scattering a mechanical wave by a fluid sphere immersed in an elastic matrix and outline the procedure to solve it and obtain its band structure.

After that, it will explore the theory for a chiral periodic array, explaining the results of future measurements and how the rotation affects wave propagation through the metamaterial.

3.1. Context

The study of acoustic or elastic wave scattering is an inexhaustible subject due in part to the endless configurations of materials in which a change of medium can occur; there are theoretical and numerical studies of wave scattering in elastic materials with inclusions of different shapes and materials, the most common being the study with solid spherical or elastic inclusions, whose change of medium generates a specific pattern in how the wave will travel through the material.

For this thesis, it is necessary to understand the wave scattering between a spherical inclusion of viscous fluid immersed in an elastic medium to expand it to a periodic configuration. This is going to be explained based on the work of Brill and Gaunaurd [14] together with the work of Psarobas [15], and then explain how wave scattering is for an elastic medium that has a helical pattern of spheres or an orthorombic structure, in order to obtain the scattering curves as in the work of Oldano and Ponti[16], all this will be developed through a plane wave expansion of the displacement field, to then form the scattering matrix.

3.2. Scattering of a viscous fluid sphere embedded in an elastic matrix

The governing equation of this type of phenomena is elastodynamic field equation for a particle displacement $\vec{u}$:

$$(\lambda + 2\mu)\nabla(\nabla \cdot \vec{u}) - \mu\nabla \times (\nabla \times \vec{u}) = \rho\partial_t^2\vec{u} \tag{3.1}$$

where λ and μ are the Lamé coefficients, and ρ is the mass density. Assuming the case where an elastic harmonic wave with angular frequency w is sent, it has the following form:

$$\vec{u}(\vec{r},t) = \tilde{u}(\vec{r})e^{iwt} \tag{3.2}$$

replacing this expression in the equation 3.1, we obtain

$$(\lambda + 2\mu)\nabla(\nabla \cdot \tilde{u}) - \mu\nabla \times (\nabla \times \tilde{u}) + \rho w^2 \tilde{u} = 0 \tag{3.3}$$

where its most general solution are two elastic waves that propagates independently from one another, one is longitudinal or irrotational and the other one is transverse or divergence-less. Following Bill and Gaunaurd's notation, the displacement $\tilde{u}$ can be written as:

$$\tilde{u} = \nabla\Phi + \nabla \times \Psi \tag{3.4}$$

and in turn Ψ can be written on the basis of Debye scalar potentials:

$$\Psi = \nabla \times r\psi + \nabla \times (\nabla \times \chi) \tag{3.5}$$

Then, substituting both expressions in the equation 3.3, the whole problem can be written in matrix form, so that proposing the type of incident wave, longitudinal or transverse, is the form that these functions will take. Therefore, it would only be necessary to establish what the boundary conditions of this problem would be in order to continue with the calculation and find an expression for the scattering matrix. The boundary conditions that have to be met for any configuration established by Bill and Gaunaurd is continuity in the displacement and in the components of the stress tensor. In this case, as the sphere consists of a viscous fluid, the elastic wave will not have the corresponding part of the shear wave, as fluids do not support shear forces on them, affecting the following material properties, amplitudes and boundary conditions:

- The shear modulus of the fluid μ is equal to zero.
- The variable x_{s2} defined as $\omega a/c_{s2}$ is infinite, as c_{s2} the velocity of the shear wave in the second material (fluid) is zero and ω represents the frequency and a is the radius of the sphere.
- All amplitudes of the shear waves associated with the sphere are null.
- Remaining as boundary conditions at $r = a$: (1) $u_r^{(1)} = u_r^{(2)}$, (2) $\tau_{rr}^{(1)} = \tau_{rr}^{(2)}$ and (3) $\tau_{r\theta}^{(1)} = \tau_{r\phi}^{(2)} = 0$.

By applying the above, it is possible to find the integer expression for the dispersion matrix for the given problem. The next step is to expand this result from a sphere to a plane that repeats periodically along the z-axis, to be able to achieve this it is suggested to follow a procedure similar to the one performed by Psarobas[15], where he in Chapter IV calculates the scattering caused by a single plane of spheres by describing the position of each of them with the following vector:

$$\vec{R_n} = n_1\vec{a_1} + n_2\vec{a_2} \tag{3.6}$$

where $\vec{a_1}$, $\vec{a_2}$ are the primitive vectors in the xy plane, and n_1,$n_2 = 0, \pm1, \pm2, ...$ The only change that needs to be made to this procedure is to add the term corresponding to the periodic repetition along the z-axis, leaving finally with a position vector with the following form:

$$\vec{R_n} = n_1\vec{a_1} + n_2\vec{a_2} + n_3\vec{a_3} \tag{3.7}$$

hereafter it is only necessary to follow the procedure outlined in the above mentioned work, taking into consideration the conditions outlined for a viscous fluid sphere.

3.3. Scattering of acoustic wave in a helical structure

To describe the helical structure, we will use the same description as Oldano and Ponti [16], where they describe the structure through a Reusch stack instead of defining a rotation with respect to the laboratory frame. As stated in the paper, the structure will be considered a plane that rotates at a certain angle as it moves along the perpendicular axis. To quantify this rotation, the parameter q will be defined as $q = \Delta\phi/d$, where d is the height of the plane we will rotate, and $\Delta\phi$ is the angle at which it will rotate. When these values tend to zero with a constant value of q, the perpendicular axes describing the plane rotate in space with a step defined as $p = 2\pi/q$, where the sign of q defines the direction of the rotation. The laboratory frame, the frame that does not rotate, is defined as:

$$x'_i = R_{ij}x_j \tag{3.8}$$

with $i, j = 1, 2, 3$, $x'_3 = x_3$ and R_{ij} is the rotation matrix. For the perturbation, if a monochromatic plane wave with wave vector $\vec{k}'$ lying in the plane x'_1,x'_3 is considered, this wave generates internal waves whose wave vectors have tangential component $\vec{k_1}' \cdot \hat{x_1}'$, causing the displacement vector to be written in the form of $u_l = u_l(x_3)exp[i(k'_1x'_1 - \omega t)]$ and the stress tensor with a similar structure, and for the propagation equation in the rotating frame results on the following expression:

$$\frac{d\vec{\beta}}{dx_3} = iB\beta \tag{3.9}$$

with $\beta = \begin{bmatrix} \vec{u} \\ \vec{\sigma} \end{bmatrix}$ and B a matrix that is defined by the set of equations that describes the propagation of the wave. It is possible to review all the explanations in the work cited above, but now let us focus on the case that interests us; since the above was for a general case, our material has a cholesteric-like structure (this means that the matrix C in the crystallographic frame (x, y, z) has an orthorhombic crystal structure) by applying this, several terms will be simplified, and it will be obtained that the longitudinal and transversal components of the vectors $\vec{u}$ and $\vec{\sigma}$ are uncoupled, and in turn that the transverse waves are coupled to each other satisfying the following equation:

$$i\begin{pmatrix} 0 & q & \nu_1 & 0 \\ -q & 0 & 0 & \nu_2 \\ -q\omega^2 & 0 & 0 & q \\ 0 & -q\omega^2 & -q & 0 \end{pmatrix}\begin{pmatrix} u_1 \\ u_2 \\ \sigma_1 \\ \sigma_2 \end{pmatrix} = k\begin{pmatrix} u_1 \\ u_2 \\ \sigma_1 \\ \sigma_2 \end{pmatrix} \tag{3.10}$$

which summarises the properties of the four normal modes $T_1^{\pm}$ and $T_2^{\pm}$, being the dispersion equation, after eliminating the stress tensor components:

$$\begin{pmatrix} C_{55}k^2 + C_{66}q^2 & iqk(C_{55} + C_{66} \\ -iqk(C_{55} + C_{66}) & C_{66}k^2 + C_{55}q^2 \end{pmatrix} \begin{pmatrix} u_1 \\ u_2 \end{pmatrix} = \rho\omega^2 \begin{pmatrix} u_1 \\ u_2 \end{pmatrix} \tag{3.11}$$

which directly give us the two following expression

1. The dispersion equation:

$$k^2 = q^2 + k_{int}^2 + \sqrt{4q^2k_{int}^2 + k_{int}^4\delta^2} \tag{3.12}$$

2. The ratio between axes:

$$\frac{u_2}{u_1} = \frac{C_{55}q^2 + C_{66}k^2 - \rho\omega^2}{iqk(C_{55} + C_{66})} \tag{3.13}$$

where $k_{int}^2 = \rho\omega^2\frac{C_{55}+C_{66}}{2C_{55}C_{66}}$ and $\delta = \frac{C_{55}-C_{66}}{C_{55}+C_{66}}$. Looking at the graph in Fig.3.1 for the dispersion relation that Oldano and Ponti made for tellurium dioxide, we get an idea of the form of this equation, if necessary in the future, is possible to measure and calculate the elements of the C-matrix of our material by resonant ultrasound spectroscopy.

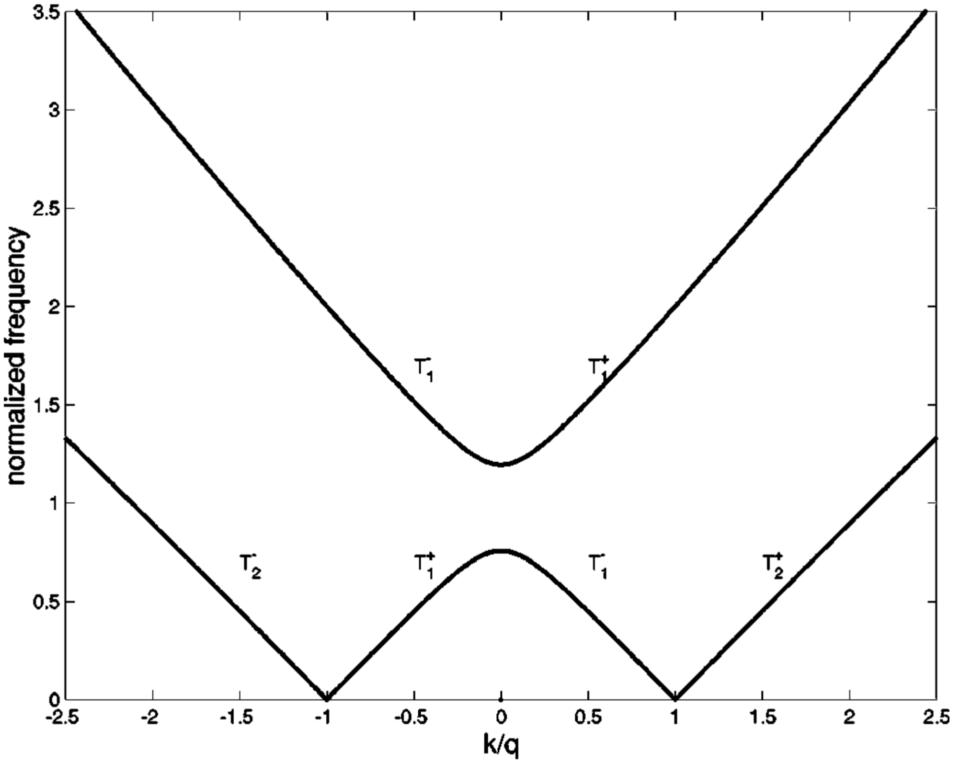

Figure 3.1: Dispersion curves from [16] for a cholestericlike structure made of tellurium dioxide in the rotating frame.

From the figure and the concept of group velocity, it is clear that certain waves are inhibited from propagating in the medium due to torsion effects; this is because T_1 and T_2

are the eigenmodes of wave propagation for this type of structures, and as they are defined, there is one of these modes, T_1, which does not transmit waves in a given frequency range. Therefore, it is expected that when we make measurements within this range, propagation for this type of waves will not appear in the measure in that specific frequency range. This highlights the complex relationship between wave propagation and the medium's structure.

Chapter 4

3D printing platform based on Rayleigh-Plateau's instability

This chapter explains the complete process for the design of the printer created, from the conceptual explanation of each physical component of the printer to the electronic components and the corresponding code created.

4.1. Context

The state of the art in 3D printing encompasses a variety of techniques, each with unique principles and applications. Among the prominent methods are Fused Deposition Modeling (FDM), where thermoplastic filaments are extruded layer by layer to form the desired object; Stereolithography (SLA), which employs photopolymerization to solidify liquid resin layer by layer using ultraviolet light; Selective Laser Sintering (SLS), utilizing a laser to fuse powdered materials, often metals or plastics, into a solid structure; and Digital Light Processing (DLP), akin to SLA but employing a digital light projector to cure resin. These techniques enable intricate designs and diverse material properties, revolutionizing industries from manufacturing to healthcare.

The proposed method for printing on elastomers presents a pioneering approach, offering capabilities not found in existing technologies. Currently, no established method exists for creating an elastic metamaterial with a periodic structure composed of viscous fluid drops. This innovative technique promises to overcome limitations in traditional elastomeric printing, potentially unlocking novel applications in soft robotics, biomedicine, and beyond. By harnessing the principles of 3D printing alongside the unique properties of elastomers and viscous fluids, this method opens avenues for developing customizable, responsive materials with unprecedented functionalities.

4.2. Viscous fluids

The goal is to recreate the Rayleigh-Plateau instability scenario explained in Chapter 2, so the first step is to decide which pair of viscous fluids to use to create our metamaterial.

First, it is known that the fluid matrix has to meet specific requirements before and after the printing process. These conditions were 1) this fluid has to have a high viscosity to trigger instability, 2) after the printing process, it has to solidify, and 3) the final solid has to be elastic enough to have the desired mechanical properties. Therefore, a polymer was the only type of material or substance that met all the criteria. However, it could not be just any type of polymer due to the original goal of shortening the build time. Polymers that meet the criteria are called elastomers, such as polydimethylsiloxane, known as PDMS, or vinyl polysiloxane, also known as VPS, among many others. Elastomers, such as PDMS, usually need a physical method for cross-linking, such as heating, UV irradiation, or chemical methods; the problem was that using a material that needs any of these procedures would only add time to the printing process, for that reason we chose to work with VPS as the matrix fluid, as this polymer has a cross-linking time τ of a couple of minutes at room temperature, fulfilling all our requirements perfectly.

The next step was to decide which fluid we were going to use for the viscous thread that was going to be destabilized into droplets; the conditions that this fluid had to meet were 1) to have a viscosity value comparable to the viscosity of the fluid matrix, 2) the density of this fluid could not be very high compared to the elastomer used, the reason for this would be discussed later in the chapter, and finally, the last condition was that the fluid had to be easy to acquire, to work with, cheap and non-toxic, concluding that the best fluid to use was glycerin.

Glycerin has an approximate viscosity of $\nu_{glycerin} = 1.43$ [Pa s], when the elastomer used has a viscosity value around $\nu_{VPS} = 2.07$ [Pa s][1], given a ratio between this values of $\nu_{glycerin}/\nu_{VPS}$ equals to 0.6813, a little less than Tomotika uses in his paper but still functional for our purpose; also, the density ratio between glycerin and VPS is $\rho_{glycerin}/\rho_{VPS} = 1,125$ (density $\rho_{glycerin} = 1261.3$ $[kg/m^3]$ and $\rho_{VPS} = 1112.1$ $[kg/m^3]$) an optimal value to have. Therefore, having decided on the fluids, we can go to the next step and drill down the design made for the printer.

4.3. Experimental Design

The experimental setup consists of three main parts that permit the simultaneous injection of several threads of fluid into a recipient full of the elastomer. As stated earlier, this allows us to control the three-dimensional structure of the constructed mechanical metamaterial by setting the parameters of the custom 3D printer.

The following parts are fixed in an MB18 aluminum breadboard (Thorlabs 457.2 X 457.2 X 12.7mm, M6).

4.3.1. Vertical Axis

The central part is a silver-plated C-profile linear actuator with a NEMA 23 motor and a Tr8*8 lead screw (p2) as a transmission method that moves up and down a structure that holds the print head. The linear actuator has a 1 m length.

---

[1] See Fig. 7.2

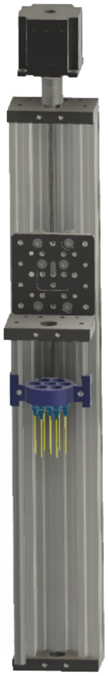

Figure 4.1: A 3D representation of the vertical axis with needles and the connector mounted in the print head.

The structure that contains the print head is 30 cm long, so the range of actual movement is around 45 cm due to the length of the needles. Motion and speed are controlled manually on the program created for this printer in the next section.

This axis is in charge of forming the threads all at once by inserting the needles into the elastomer container and then extracting them. At the same time, the fluid is injected with the fluid extruder, forming the thread in equilibrium that is needed for the instability to occur.

4.3.2. Horizontal Axis

This axis is also a silver-plated C-profile linear actuator with a NEMA 23 motor and a Tr8*8 lead screw (p2), whose length is 25 cm. The moving plate has a structure that holds the recipient with elastomer in place.

The container is mounted on a movable plate because when a sample was printed before installing this axis, each thread split the instability at a different time, leaving seven threads whose distances between drops and drop sizes were the same, but all in different planes, not leaving the desired periodicity in the vertical axis.

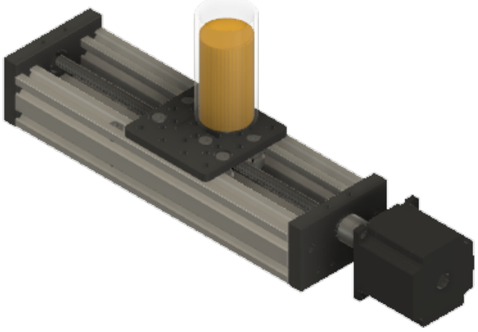

(a) A 3D representation of the horizontal axis with an elastomer container

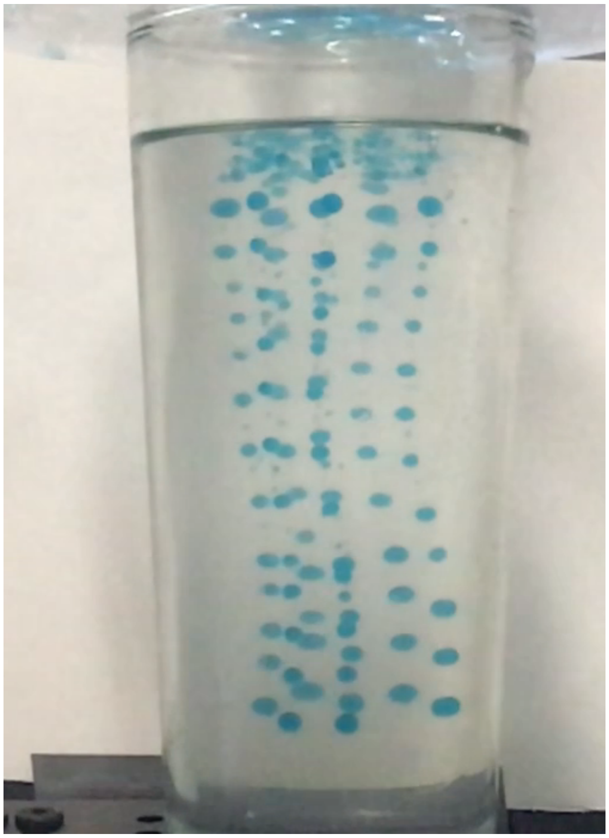

(b) Frame of a video where a sample is being printed without the implementation of the horizontal axis motion, where drops of similar sizes and separation can be seen, but located at different z-planes.The elastomer used is PDMS and the fluid inyected is glycerin with blue ink.

To fix this issue, we use the idea proposed by Cai, Brun, and Marthelot [17], where they unravel a way to control the spacing between the drops by moving the nozzle in a sinusoidal motion because doing so sets the drops on the nodes of the sinusoidal. In our case, we adjusted this finding. We chose to only add a zig-zag motion at the base, which, when coupled with the movement of the vertical axis, would form a triangular wave with the fluid thread, the fixed wavelength being equal to the amplitude of the zig-zag movement, as can be seen in Fig.4.2.

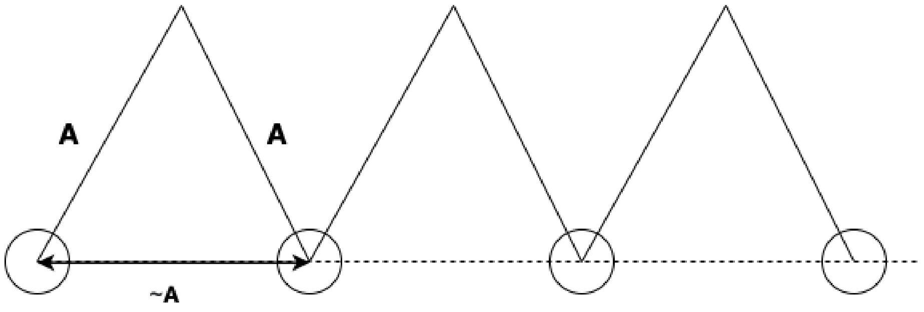

Figure 4.2: Diagram of the path followed by each nozzle when joining the movement of both axes.

The above statement is true in most possible configurations, except when the triangular wave is flattened. This occurs in two cases: the first is when the frequency of the zig-zag movement is shallow and/or the extraction speed is not high enough, and the second case is when the diameter of the thread being formed is larger than the movement of the base, as this causes the thread not to perceive the movement. We have to be clear about why we want to add this process: by zig-zagging the fluid thread, we are forcing it to break at the weakest points; if we see Fig. 4.2, we notice that the breakage happens at the top of the triangle because this is the farthest point from the original path of the thread and added to the inertia of wanting to return to it, the thread will separate into drops, as expected by the instability, but remaining fixed at these new points.

4.3.3. Fluid extruder

The fluid extruder comprises two parts, each with a specific purpose but very editable features: the first part corresponds to the device that puts the fluid inside the elastomer, and the second corresponds to the connector between needles and the first device. As said before, this device is in charge of injecting the fluid into the fluid matrix, and it can be modified according to the characteristic that wants to be exploited. One device option is a syringe pump with the same number of syringes as needles needed; this would be connected to the needles through silicone hoses and the designed connector. This option is recommended if precision in the flux injected is wanted; the only disadvantage is that it would require more space around the printer.

The other option for fluid injection is to make a device similar to a "syringe pump" mounted on the print head structure, the design that emerged is to make two pieces joined by a worm screw that is attached from below a container with the connector at one end, the container used was a 150 ml syringe where the tip was cut in order to attach the connector, and from above a movable piece by the lead screw that when moved will push the plunger to a certain distance causing a certain amount of fluid injected. A NEMA 23 motor will handle the above movement on top of the print head. The advantage of this design was the minimal use of space. Since the structure was mounted on the print head, the printer would need less mounting space. However, the problem with this design was the possible need for more accuracy in the injected flow rate since it is necessary to thoroughly calibrate how much fluid is injected when the motor moves a certain amount of steps.

Both designs were used, but we opted to continue working with the first option because we wanted to eliminate as many sources of error in the printing process as possible. Therefore, we used two vacuum pumps: a NE-1600 six-channel and one NE-1000 one-channel programmable syringe pump, both from New Era Pump Systems.

The other part of the fluid extruder consists of the connector between the container or hoses and the needles; the importance of this connector is that it defines how the needles are arranged and, therefore, the final arrangement of the droplet plane. It depends on the user the shape that this connector can have; if it wants to have a circular shape with seven or fewer spaces for needles as seen in Fig. 5.3, it can be a linear or rectangular arrangement, it will depend on the shape of the desired metamaterial, once the design is ready, it can be printed with PLA in a standard 3D printer.

The connector used in this thesis is the one shown in Fig. 4.3.a, in the form of a 7-needle honeycomb; in the next chapter, we will characterize the shape of the unit cell of the samples. Moreover, the needles used are made of stainless steel with a 2.5 mm internal diameter, 30 cm length, and a blunt tip from Dispense All.

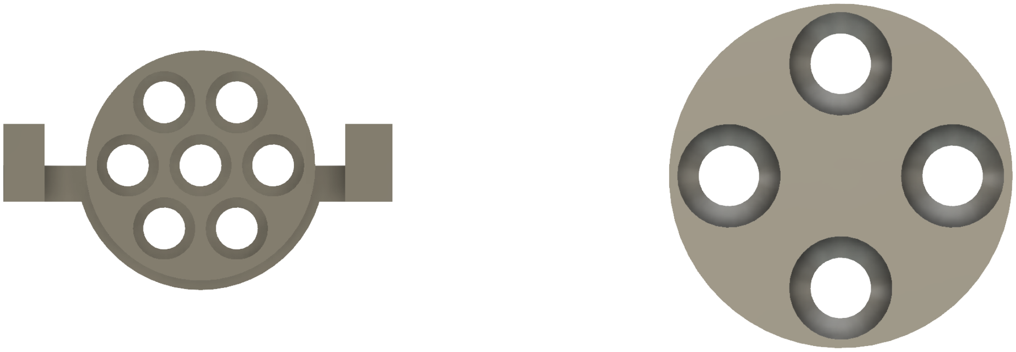

(a) For 7 needles in the shape of a honeycomb.

(b) For 4 needles in a square shape.

Figure 4.3: Top view of 3D design connectors

4.4. Program design

The next and final step in the printer design consists of building the electronic circuit and creating the code that would allow us to control the printer as interactively as possible. As said before, step motors control the axis, precisely NEMA 23 that connected to a micro step driver and a power supply would move both the print head and base of the printer; usually, when a step motor is used, the simplest way of controlling it is by using an Arduino board, it is very accessible and friendly to the user, for this reasons in the begging an Arduino MEGA 2560 board was used to control both motors. However, soon enough, a severe problem was encountered: as both motors were controlled by one device, the changes made in the movement of one would affect the other, making it almost impossible to test one variable at a time, as the program is going to build step by step, meaning that, for example, a change in the amplitude of the horizontal axis would mean a change in the time that the motor would take to move to each side, affecting the overall time that the printer it would go up. The solution we found for this problem was to change the controller from an Arduino to an ESP32 board; the reason behind this decision will be explained in the next part.

4.4.1. Electronic Components

The electronic components used to build the printer are the following:

- **For the vertical axis**: A NEMA 23-step motor, a micro-step drive DM542, a power supply Mean well 24V/14.6A/350W
- **For the horizontal axis**: A NEMA 23-step motor, a micro-step drive DM542, a power supply Mean well 24V/14.6A/350W
- **For the fluid extruder, option 1**:A NEMA 23-step motor, a micro-step drive DM542, a power supply Mean well 24V/14.6A/350W
- **For the fluid extruder, option 2**: A NE-1600 and NE-1000 syringe pumps

- **For the controller**: An ESP32 board, an LCD screen 1602A, an interface I2C, a keypad, a protoboard, and jumper wires.

In this case, it is not necessary to have three power supplies to power up the step motors; it is enough with just one of them. The connection is straightforward; both motors are connected to their respective drivers and, through them, to the ESP32 board. Also, they are connected to the power supply. The keypad is connected to the board using the jumper cables and the protoboard, and in order to minimize the pins used by the LCD screen, the I2C module is soldered to the screen, causing only two pins needed instead of the original six pins.

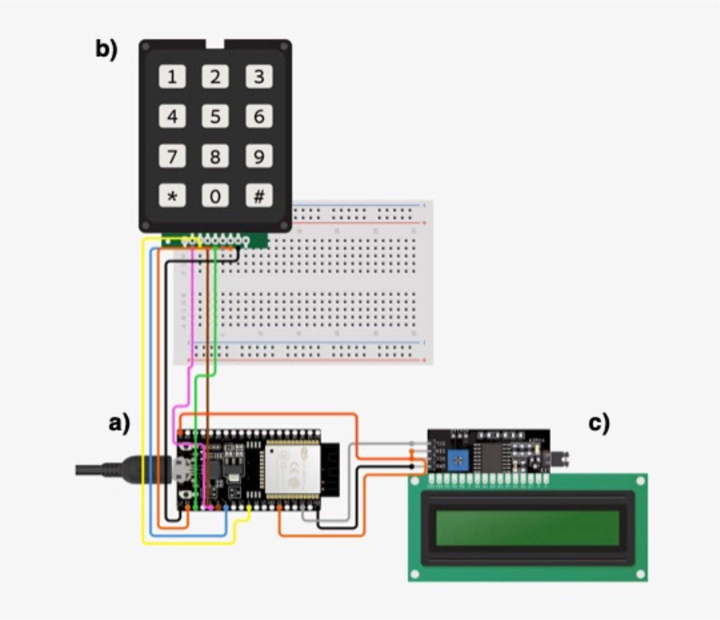

Figure 4.4: Schematic of electrical components connections: (a) ESP32 board, (b) Keyboard 4x3 and (c) LCD Screen with I2C module.

Once everything is set as Fig. 4.4 shows, we can explain why these components were chosen: the decision to use NEMA 23 motors was simply for the force needed to move the print head and the recipient at a sufficient speed; the most important resolution was changing the controller from an Arduino to an ESP32 board, this was to solve the interlacing problem between both movements, as, unlike an Arduino, it has two cores that allow separating the work of both axes in each core, without interrupting the other, this would allow simplifying the programming because it would only be necessary to focus on the work of one axis at a time and then combine them to create the desired product. Furthermore, the keypad and LCD screen were added to facilitate the user's understanding and use of the printer, as the keypad would give the user the order to execute a defined task. The screen would show the details of the executing task.

4.4.2. Code

The program was written in C++, and the libraries used were *Arduino*, *LiquidCrystal_I2C*, *Keypad*, and *Stepper*, each to control the corresponding electronic component; the code was a structure in 3 significant parts: the first one correspond to the setup of the keypad, the component in charge of giving the program the events to use, the second one is the creation of steppers movements, forward and reverse functions, and the third is the set up of the loop, the part of the code in charge of putting together the movement of both motors in order to create the metamaterial.

One of the advantages of putting a keypad to control the printer was the versatility given by the smaller number of pins utilized. The printer is built as a finite-state machine with two primary states: Waiting and Looping. In the first state, the printer can execute any event that the user wants; these events are finite in time, they can be used by one or the two cores of the board and are triggered by a specific key, as can see in lines 108 to 127 of the code in Appendix D; in the printer code attached, only six keys were used, four were used to define the forward and backward functions of the motors and be able to manual configured the initial position, one to change the state from Waiting to Looping and the last one to reset the printer back to the Waiting state.

The second state puts the printer in a loop; this loop is the complete printing process. It puts the motors moving in their specified configuration, each axis with its given speeds and the horizontal axis with its given amplitude. As the printing process only lasts a few seconds, it is necessary to have a way to break the loop and bring the printer back to the standby state, and that is why a reset button was added to the program. This button also works to minimize the latency of the cores; although the board has two cores that can work simultaneously, this does not imply that both present the same response speed. These cores are arranged by priority; core number 1 has a faster response than core 0; for this reason, the movement of the vertical axis was configured in this core, as it was needed so that it would not present delays in its operation.

Now, the keyboard used on this occasion was a 4x4 keyboard. This means that we still have 12 keys to potentially use in our program to create an event or save a configuration just by adding a case to the program. This makes the program scalable because to change from one configuration or case to another, it is not necessary to disconnect the printer or reload the program, but it can be saved in extra cases.

Chapter 5

Tomographic sample characterization

This chapter explains the final configuration of the metamaterials created. It involves measuring the relevant distances to characterize each sample and connecting these distances with the printer's parameters. To achieve this, we will use images of the internal structure obtained by tomography. Furthermore, we will detail the internal structure of the samples from their unit cell.

5.1. Context

Given the entirely novel nature of the printing process proposed, establishing a clear conversion framework between the printer's parameter settings and the resultant product became imperative. This mainly pertains to determining the size of the droplets and the spacing between them, which are crucial factors in defining the printed material's structural integrity and functional properties. Developing precise correlations between the printer's parameters and the desired characteristics of the final product required meticulous experimentation and analysis. Such efforts facilitated the optimization of printing parameters for achieving desired outcomes and provided insights into the underlying physics governing the interaction between the printing mechanism and the material properties. Consequently, this calibration process played a pivotal role in ensuring the reproducibility and reliability of the printing method, laying a solid foundation for its further advancement and practical implementation in various applications.

In order to measure distances and effectively characterize each sample within the polymer, the acquisition of images is imperative. However, the inherent non-transparency of the polymer poses a significant challenge in obtaining clear and accurate images using conventional methods. Consequently, a specialized image-obtaining technique becomes essential to surmount this obstacle and extract meaningful data from the samples. The chosen method to address this challenge is Computerised Tomography (CT), a sophisticated imaging technique widely employed in various fields, including medicine, engineering, and materials science.

Computerized Tomography, commonly known as CT, is a non-destructive imaging technique that utilizes X-rays to create detailed cross-sectional images of objects. It operates on the principle of attenuation, where X-ray beams are projected through the object from multiple angles. As the X-rays pass through the object, their intensity diminishes depending on the density and composition of the materials they encounter. By capturing X-ray attenuation data from multiple angles around the object, a computer algorithm reconstructs a three-dimensional image that represents the object's internal structure with high precision.

In the context of polymer characterization, CT imaging offers a powerful means to visualize and analyze the internal morphology of samples, providing valuable insights into their composition, structure, and spatial distribution of components.

5.2. Internal Structure

The structural dynamics of the system elucidated in the preceding chapter reveal a nuanced architecture comprising seven distinct threads of drops, each characterized by an identical diameter, d. The internal arrangement is defined by the separation denoted by the variable c between successive threads. Each drop within these threads is located precisely on a designated plane, and the inter-plane spacing is symbolized by the variable A. The size of the individual droplets is closely linked to the velocity along the vertical axis and strongly influenced by the flow rate injected, highlighting the dynamic nature of the system components.

In addition, the separation A between the planes is intricately governed by the amplitude of the zig-zag movement executed by the horizontal axis. This nuanced interplay between the horizontal and vertical movements underscores the intricacies of the system's spatial organization. The amplitude of the horizontal axis's zig-zag motion serves as a critical determinant in regulating the spatial arrangement of the planes, thereby directly influencing the system's overall structure and dynamics. The above can thus be seen in Figure 5.1, where each distance is represented. Understanding these interdependent variables is essential to understand the underlying mechanisms governing the system's behavior and to create new structures effectively.

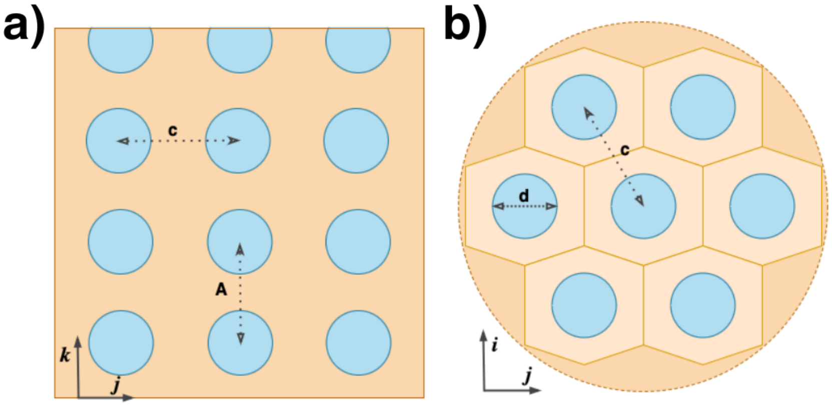

Figure 5.1: Representation of a sample, with the orange part being the fluid matrix or polymer and blue part the viscous fluid injected. a) Transversal cut of a sample showing the repetition in the z-axis of the plane with drops. b) Plane cut with a hexagonal arrangement of unit cells.

5.3. Tomography

The CT imaging process was conducted using the BioCT Brüker Skyscan 1278, situated at the Faculty of Odontology of the University of Chile, and made possible through funding from the FONDEQUIP EQM 150010 project. This state-of-the-art equipment facilitated the acquisition of high-resolution images with a $50\mu m$ cubic voxel size of spatial resolution, essential for detailed analysis of the polymer samples under study. Each imaging session spanned between 30 to 40 minutes, during which the BioCT Skyscan 1278 meticulously captured the internal structure of the samples with remarkable precision and fidelity.

Following image acquisition, the operator meticulously processed the data, resulting in a comprehensive set of 1000 images for each sample, capturing various slices. Subsequently, the dataset was made available for analysis through three specialized software packages: CTvox, CTAn and Data Viewer.

Figure 5.2: Screenshot of the CTvox software showing the reconstruction of one of the constructed samples.

CTvox facilitated the three-dimensional reconstruction of the sample, providing researchers with a holistic view of its internal structure as seen in Fig. 5.2. CTAn was pivotal in delineating the analysis area, particularly in identifying the precise locations of the drops within the sample. Additionally, Data Viewer provided various cuts, enabling researchers to measure the distances between drops and their diameters, thereby enabling a thorough sample characterization based on the parameters intrinsic to the printer's operation. Integrating these advanced imaging techniques and software tools underscores the meticulous approach adopted in characterizing the polymer samples and unraveling their complex internal dynamics.

The measurement process was conducted systematically to ensure accuracy and reliability. Initially, slices containing the maximum number of drops, extracted from Data Viewer, were selected for analysis using Matemathetica. In Matemathetica, the images were transformed into binary format to identify and isolate the drops within the image, laying the foundation for precise measurement and analysis.

To ascertain the distances between drops or planes denoted by 'A,' the coordinates of each drop were meticulously extracted, facilitating the calculation of distances using a standard distance formula: $d = \sqrt{(x_2 - x_2)^2 + (y_2 - y_1)^2}$. This iterative process was repeated across five samples, each with distinct parameters, allowing for a comprehensive understanding of the spatial arrangement within the samples under varying conditions. Moreover, the following methodology was employed to determine the diameter of the droplets: The area covered by each droplet was encapsulated within a circumference, and droplet diameters were derived by exploiting the established area expressions.

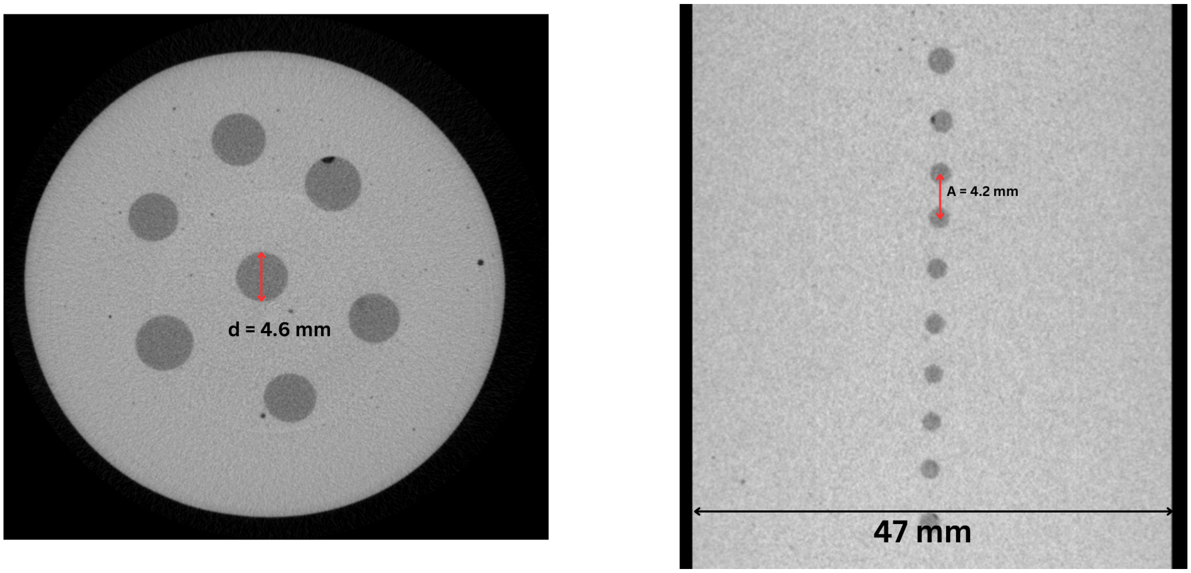

(a) Coronal section of a sample from the Data Viewer software.

(b) The sagittal section shows a thread of droplets from a sample in the Data Viewer software.

Figure 5.3: Two different cuts of a sample were obtained thanks to the Data Viewer software.

The five samples' measurements will be presented in the following table, with their specific characteristics.

Table 5.1: Summary table of measured samples with their print parameters together with measured distances.

N^o samples	A_{set} (mm)	$A_{measure}$ (mm)	u (cm/s)	Q (mm^3/s)	d (mm)
1	4.0	4.2	0.58	3.3	1.16 ±0.15
2	4.0	4.3	0.58	8.3	1.59 ±0.16
3	4.0	4.1	0.41	3.3	1.21 ±0.19
4	2.5	3.8	0.46	3.3	1.22 ±.28
5	2.5	5.0	0.46	8.3	1.90 ±0.41

The visual representations in Figures 5.4 and 5.5 encapsulate the measurements and analysis performed on the polymer samples. Figure 5.4 clarifies the direct relationship between the instability wavelength and the printer's horizontal axis motion amplitude. Despite variations in the size of the initial threads or droplets, the measured distances remain uniform across three different samples, for an original value of A1 = 4 mm. This observation underlines the fundamental role of the amplitude of the horizontal axis motion in the control of the instability wavelength, without leaving in consideration that this control starts from values of A similar or more significant than the instability wavelength for initial thread size.

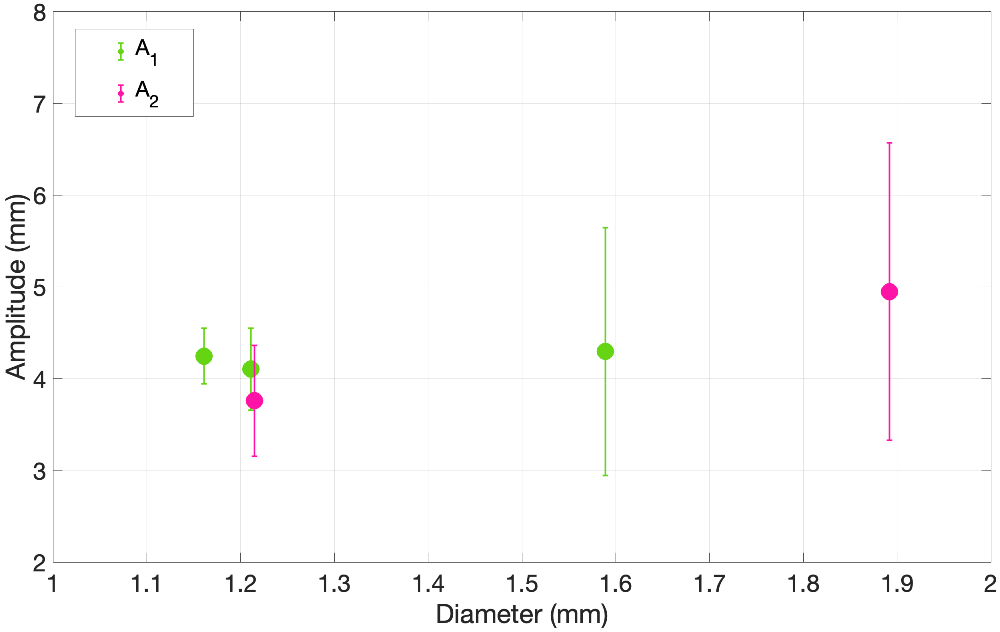

Figure 5.4: Distance measured between planes, A, in function of the diameter of 5 samples, with $A_1 = 4$ mm and $A_2 = 2.5mm$.

In contrast, Figure 5.5 provides insight into the relationship between droplet diameter and the velocity of the injected fluid stream, with a particular focus on flow rate dependence. The graph highlights how variations in fluid stream velocity yield similar droplet diameters, underscoring the dominant influence of the injected flow rate in determining droplet size. Regardless of the velocity at which the fluid is injected, the resulting droplet diameters remain comparable, indicating that the volume of fluid delivered, as determined by the flow rate, dictates the size of the droplets.

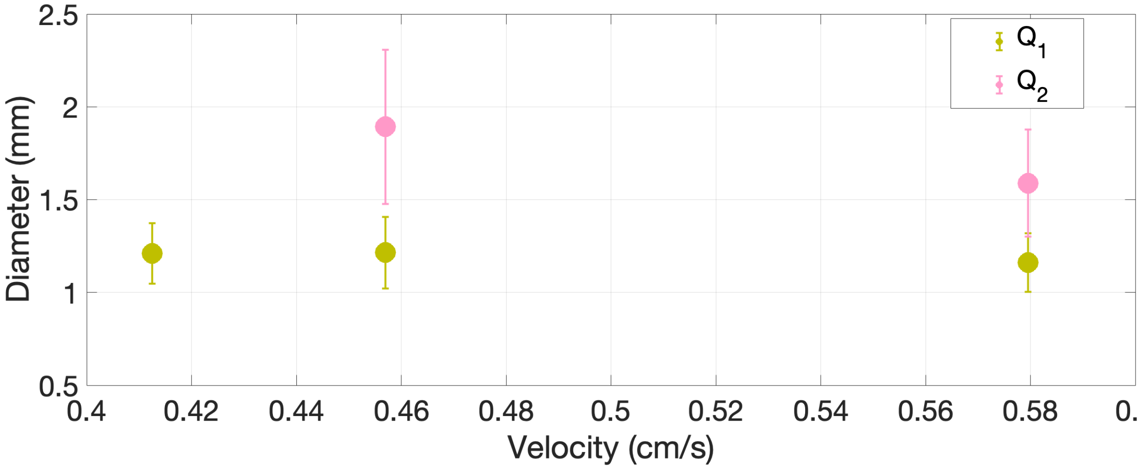

Figure 5.5: Droplet diameter as a function of velocity and flow rate injected for the 5 samples, with $Q_1 = 3.3\ mm^3/s$ and $Q_2 = 8.3\ mm^3/s$.

In our approach, while drawing inspiration from the work of [17] regarding fixing drops in the same plane, key distinctions arise in the method of drop formation and subsequent size determination. Unlike their methodology of jetting, where the fluid is injected unidirectionally with the entire head moving perpendicularly, our process involves simultaneous injection and movement in the same direction. As a consequence, the size of the droplets primarily hinges on the injected flow rate and the head movement speed, diverging from the sinusoidal motion parameters influencing drop size in their model. This discrepancy becomes evident in our experimental results, as illustrated in Figure 5.6, where the diameters measured through tomographic images and the theoretically predicted values are shown.

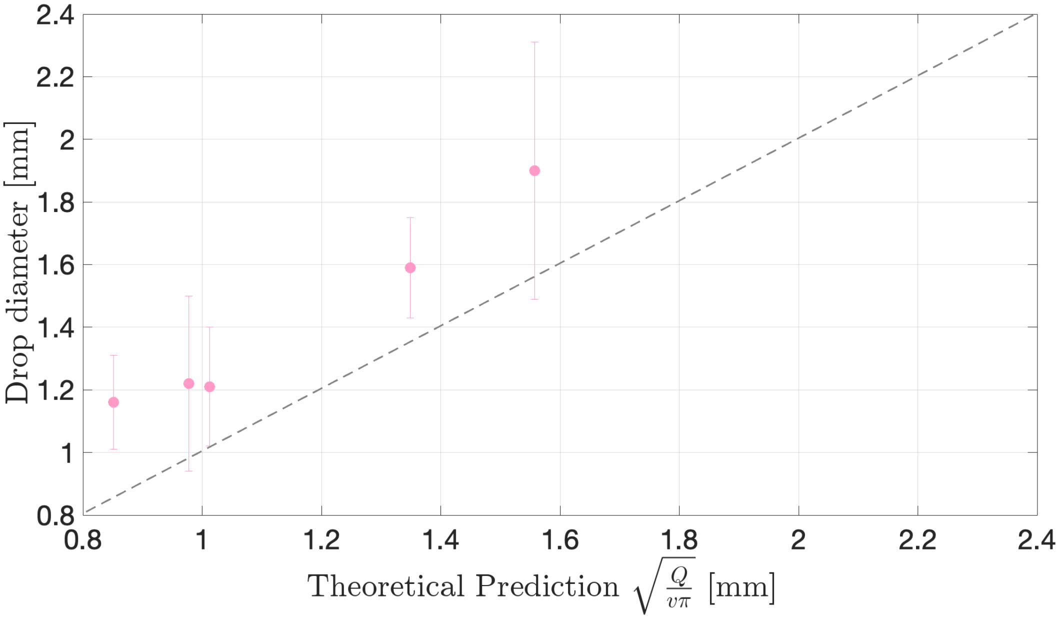

Figure 5.6: Droplet diameter calculated compared to the theoretical prediction for the 5 samples.

Chapter 6

Acousto-Mechanical Measurements

This chapter will showcase two different experimental responses of our mechanical metamaterial samples. The first part will explain both experimental setups that were made to characterize the metamaterials, explaining each of their parts and the instruments used. Then, it will pass to the results obtained, separated into two important sections: according to their internal structure and according to the external actuation.

6.1. Context

Having completed the meticulous construction, creation, and characterization of the samples, we have thoroughly understood their inherent properties, including their characteristic sizes and structural nuances. The current focus of our research is to elucidate how these samples respond to mechanical waves, a fundamental step in unraveling their dynamic behavior under different stimuli. To achieve this, we are entering the field of acoustic measurements, which offers numerous techniques for probing material properties and wave interactions.

Acoustic measurements constitute a cornerstone in studying mechanical wave behavior, offering diverse methods to interrogate material properties and wave propagation characteristics. Among the state-of-the-art techniques are Impulse Excitation Technique (IET), providing non-destructive evaluation of material elasticity and damping properties; Laser Doppler Vibrometry (LDV), enabling high-resolution measurements of surface vibrations with laser beams; and Acoustic Resonance Spectroscopy (ARS), utilizing resonant frequencies to assess material composition and structural integrity. In this study, however, we employ acoustic spectroscopy, leveraging the interaction between mechanical waves and the material to glean insights into its elastic and viscoelastic properties. The proposed future direction involves Digital Image Correlation (DIC), a powerful optical technique offering precise surface deformation measurements under mechanical loading, complementing the information obtained through acoustic spectroscopy and enriching our understanding of the samples' mechanical response.

6.2. Experimental Setup

The measurements were carried out in two different configurations, each for a different purpose, as described below, and the data were taken in each case in a different way.

6.2.1. Internal structure

Smaller samples, around 10-12 cm, were mounted in a screw press to keep them fixed. At one end, a mechanical vibrator Brüel & Kjaer Model 4810 was positioned to force a vibration on the sample and to measure the transmission at the other end with a shear accelerometer PCB Model 352C22 connected to an ICP sensor signal conditioner Model 480E09. The shaker was controlled by a 2-channel network signal analyzer Stanford Research Systems Model SR780, which performs a sweep sine measurement with maximum amplitude of 0.1 mV_{pk} from 50 Hz to 2500 Hz to have the material's response, see Fig. 4 in Annex F 7.1. In simple words, this equipment creates a list of frequencies in the chosen frequency range, which will be evaluated in the sinusoidal signal sent, $s(t)$, to the mechanical vibrator; the other channel will receive the output signal of the material, $r(t)$, which will be subjected to various analyses within the equipment and then delivered to the user. These analyses consist of making a Fourier transform to the received signal that depends on the time so that it depends on frequency and can be compared with the sent signal. Once the signal is in the frequency domain, the magnitude of each frequency component is calculated. This magnitude represents the signal amplitude at each frequency point and is usually normalized to a reference amplitude. Then, the transfer function $H(f)$ is derived by dividing the power spectra of output magnitude response by the power spectra of input magnitude response at each frequency point, represented as a complex function of frequency

$$H(f) = \frac{|\hat{r}(f)|}{\hat{s}(f)} \tag{6.1}$$

Finally, it can be plotted graphically, with frequency on the x-axis and either magnitude or phase (or both) on the y-axis. This graph concisely represents how the system responds to different frequencies.

The data was obtained using a Matlab script that graphs the transmission function and the amplitude of the sent signal and the received input and output signals.

6.2.2. External Actuation, specifically degree of helicity

The experimental setup for the larger samples, around 25 to 30 cm, consists on:

1. Two cylindrical acrylic parts with an inner radius of 5 cm, an outer radius of 6 cm, and a width of 2 cm. On the flat face 5.8cm from the origin, it has 30 threaded holes for M4 screws, located on the sides and diametrically symmetrical with a 6° separation between them. It also has a recess centered at 5.3cm from the origin, 2mm wide, and 4mm deep. On the curved surface, it has 6 M6 holes located perpendicular to the center of the threaded holes, with a spacing of 22.5° between them.

2. Four rectangular stabilization bars are 20 cm long, 1.5 cm wide, and 0.8 cm high. They have two holes with a 7 mm radius, 15 cm apart. In the center, there is an opening 8 cm long and 6 mm wide for fixing an M6 screw; at the same height, there are two tabs 4 mm wide and 5 mm high, which help to keep the cylindrical pieces parallel to each other.

3. Four pieces were designed as clamps to fix the samples to the cylindrical pieces, consisting of half-cylinders 5 cm in diameter, 5 mm wide, and 1 cm high, from the ends of which two extensions of 3. 5 cm long, 5 mm wide, and 4 mm high, which are used to fix the

sample to the structure in the desired position, since it has an M4 hole at the end, with this union it can control the level of helicity of the structure; the first 8 mm of this extension is a square structure with an M6 hole in the middle, which serves to join both pieces and tighten the sample so that it does not move.

4. The whole structure is fixed to a Thor-Labs MB2020/M Aluminum Breadboard, 200 mm x 200 mm x 12.7 mm, M6 taps, with 4 Thor-Labs TR8 optical posts, 200 mm long. With a pair of posts, one end of the structure can be made by putting the cylindrical acrylic piece between two stabilization bars. Then, it is necessary to set each of these ends 15 cm apart.

5. To finish this part of the experimental setup, the clamps must be attached to the sample and fixed to the structure.

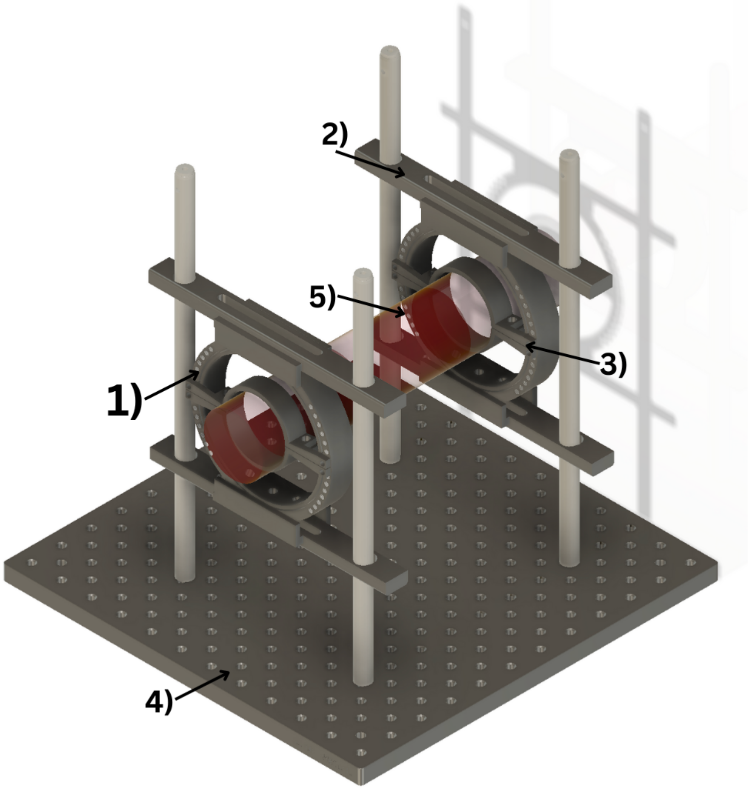

Figure 6.1: 3D representation of the experimental measurement setup: #1 indicates the pieces that allow the rotation of the samples, #2 indicates the fixers that keep the system immobilized, #3 are clamps designed to hold the piece and allow the rotation of it, #4 is the breadboard where everything is assembled, and #5 is a representation of the sample.

A Gaussian pulse is sent for these measurements and the internal frequency changes. To create this signal, Matlab is used, and through a NI GPIB-USB-HS acquisition card, an Agilent 33220A function generator is controlled, which is connected to a Sinocera YE5871A power amplifier, which in turn is connected to a Sinocera JZK-10 mechanical vibrator that is in contact with one end of the sample, mounted on the structure described above, at -45°, 0° and 45° measure from the vertical axis. 3 PCB Model 352C22 accelerometers connected to an ICP Model 480E09 sensor signal conditioner are used to capture the material's response. These sensors are connected to a Stanford Research Systems Model SR560 low noise preamplifier to filter the signal from those frequencies lower than 10 Hz and higher than 1 kHz to have a cleaner signal and amplify it to be able to study it. Then, the signals are passed to an NI USB-6218 acquisition card to obtain the results back to Matlab. Finally, the responses are graphed and saved as text files here.

The first accelerometer is at one end of the sample, aligned with the mechanical vibrator to identify the wave being sent. The second accelerometer is positioned 19 cm away on the sample's surface, and the third accelerometer is also positioned at the same distance but at a 90° angle from the line defined by the previous accelerometers. Three signals are received, one for each occupied accelerometer. The data is analyzed with Python, and a code is created to calculate the envelopes of each measurement, that is, to determine the group velocities using the time-of-flight technique, where we will measure the time it takes for the sent pulse, the maximum amplitude of the envelope signal, to reach the end of the material. Having the distance that separates the two sensors and seeing the time difference with which they arrive, the group velocity can be calculated for each signal sent.

6.3. Results

In this section, we present and analyze the measurements obtained for each type of characterization. Each measurement provides valuable information about the material's properties and behavior, enhancing our understanding of its structural dynamics. By examining these measurements, we aim to display the mechanical characteristics of the 3D-printed material and their implications for the propagation of acoustic waves.

6.3.1. Characterization by the internal structure

Figure 6.2 completely represents the entire measurement data, providing critical insights into the material's behavior. It plots the signal amplitude sent (Fig. 6.2.a), ensuring uniformity across all samples regarding the waveform transmission. Concurrently, it depicts the amplitude of the received signal. It offers valuable information regarding the frequencies at which the accelerometer ceases to receive data or indicates anomalies within the material's internal configurations. Any unusual boost in amplitude within specific frequency ranges can indicate noteworthy behaviors within the material. Moreover, the transfer function defined as Fig 6.2.b over Fig 6.2.a, as showcased in Figure 6.2.c, represents the normalized response of the material under a given forcing.

A crucial measurement was performed on a sample composed of Elite Double 22 polymer, devoid of any fluid droplets, to establish grounds for comparison with other samples. This step was imperative to discern the polymer's inherent characteristics and response mechanisms in its pure form.

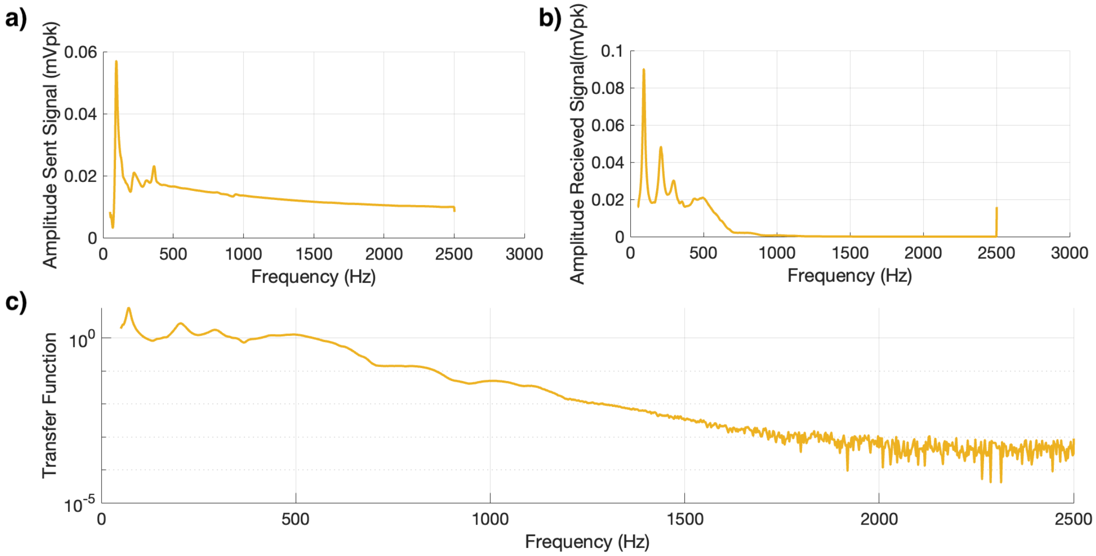

Figure 6.2: Graph showing the entire measurement, the amplitude of the signal sent and received together with the transfer function.

By analyzing the material sans any additives, we gain valuable insights into its intrinsic properties and behavior, thus facilitating a more nuanced understanding of how the introduction of fluid droplets alters its dynamics. This baseline measurement serves as a reference point against which the behaviors of composite samples can be evaluated and interpreted, enabling a comprehensive analysis of the impact of fluid inclusion on the material's response.

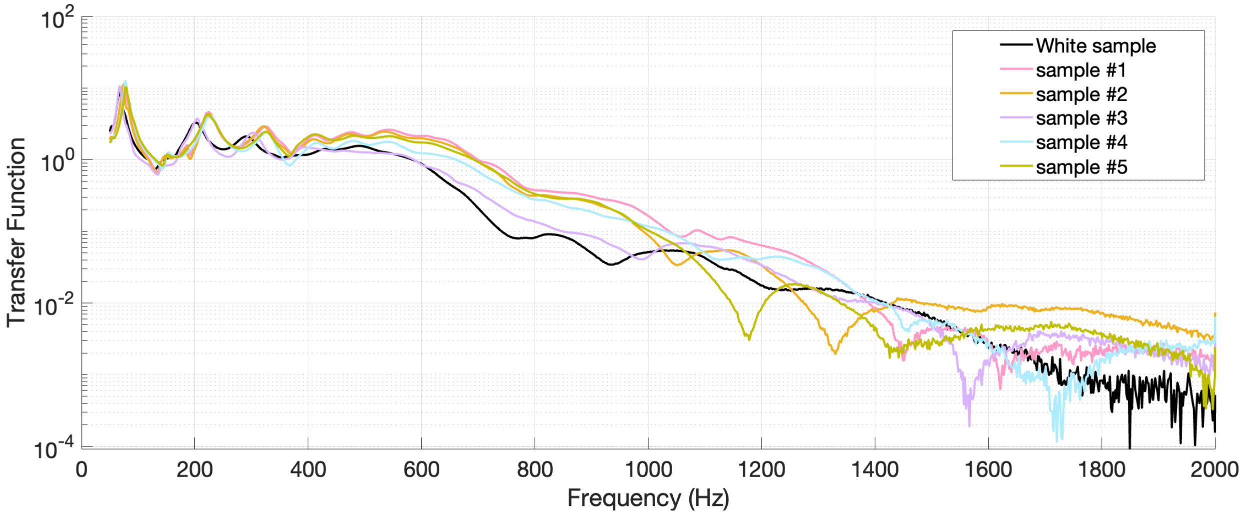

Figure 6.3: Transfer function for different samples, characterized in 5.1 in the previous chapter, created compared to a blank sample in a frequency sweep from 0 to 2000 Hz.

The first tests conducted were to observe the frequency response of the metamaterials created by manipulating their internal structure through control parameters. This exploration aimed to discern how parameter variations such as droplet size and separation between them influence the material's band structure. By systematically altering these parameters, we sought to anticipate shifts or changes in the material's band structure, thereby gaining crucial insights into its dynamic response to different configurations.

The measurements yielded insightful results, see in Fig. 6.3, particularly in comparing the frequency response of two distinct samples alongside a blank sample. Our analysis revealed the presence of two absorption bands in the sample characterized by smaller droplet size and wavelength, named sample N° 1, whose characteristics are shown in Table 5.1 (depicted by the pink line). Interestingly, these bands exhibited a leftward shift as the droplet size and wavelength increased, as evidenced by the green line representing sample N°5. Our interpretation of this band structure behavior suggests that the frequency of minimal transmission decreases for larger droplet sizes and increased separation. In particular, for larger droplet sizes, such as sample N°2, the orange line with a minimal transmission point between the samples named before has a similar separation between its drops to sample N° 1 but varies in droplet diameter.

These measurements were only considered until 1600 Hz, as the amplitude of the received output signal started to mark 0 from this frequency, due to the damping of the material.

6.3.2. External Actuation

6.3.2.1. Degree of Helicity

As mentioned in the context, the objective of these measurements is to understand the dynamic behavior under different stimuli. Since the samples are made of a compliant material, it is possible to modify their responses by applying external forcing. They can be squeezed, stretched, or rotated, the latter option being the most ideal since the material's wavelength is not significantly modified.

However, to see if this proposal makes sense and modifies wave propagation, we did a mini-test before scaling this idea further, so in the second phase of our experimentation, we embarked on tests and classifications to understand the frequency response of the samples by varying their orientation by rotation or by converting them into a helical structure. To perform this measurement, we used a combined configuration in which the sample was fixed inside a structure described in Section 6.2.2. Despite this alteration, the signal sent remained a similar frequency sweep signal to that of the first test, which ensured the consistency of our experimental approach.

The measurements conducted in this phase yielded the following results, seen in Fig. 6.4. We observed distinct behaviors in the sample's frequency response as its helicity was manipulated. For instance, in the absence of rotation, the sample exhibited a minimum transmission at frequencies around 70-75 Hz. However, as the helicity of the material increased, these frequencies began to allow the transmission of waves through the material, indicating a shift in its response characteristics. Conversely, we observed an opposing behavior in certain regions, further underscoring the complex interplay between the sample's orientation and frequency response. These findings offer valuable insights into the material's dynamic behavior under varying conditions of orientation and helicity, shedding light on its potential applications in tunable and responsive systems.

The investigation into the material's band structure reveals a dynamic response at low frequencies and higher frequencies, indicating a nuanced sensitivity across a broad frequency spectrum.

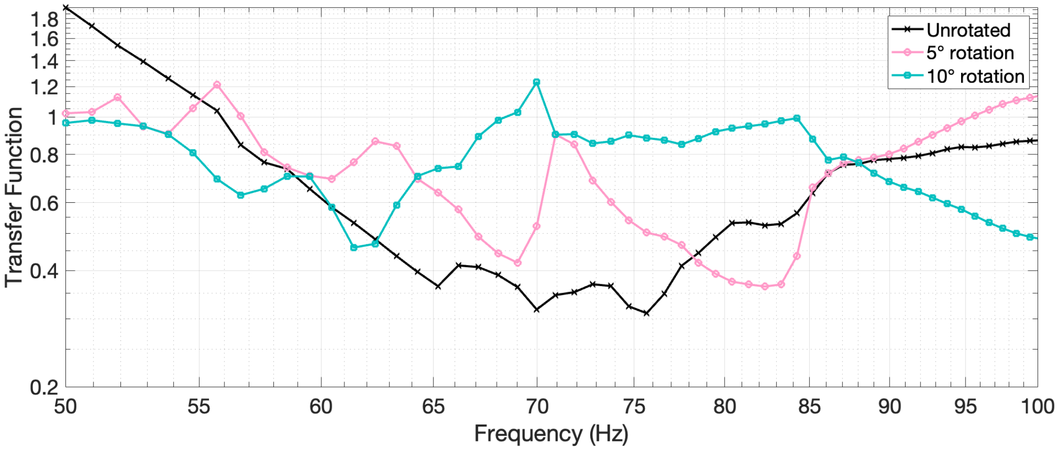

Figure 6.4: Transfer function, for low frequencies, obtained by rotating a sample at different degrees and sending a longitudinal wave through it.

Notably, in Fig. 6.5 at 250 Hz, we observe a recurrence of the previously identified behavior, further underscoring the material's adaptability and responsiveness to varying frequency regimes. This consistency in the observed behavior across different frequency ranges suggests a fundamental relationship between the material's internal structure and frequency-dependent response mechanisms.

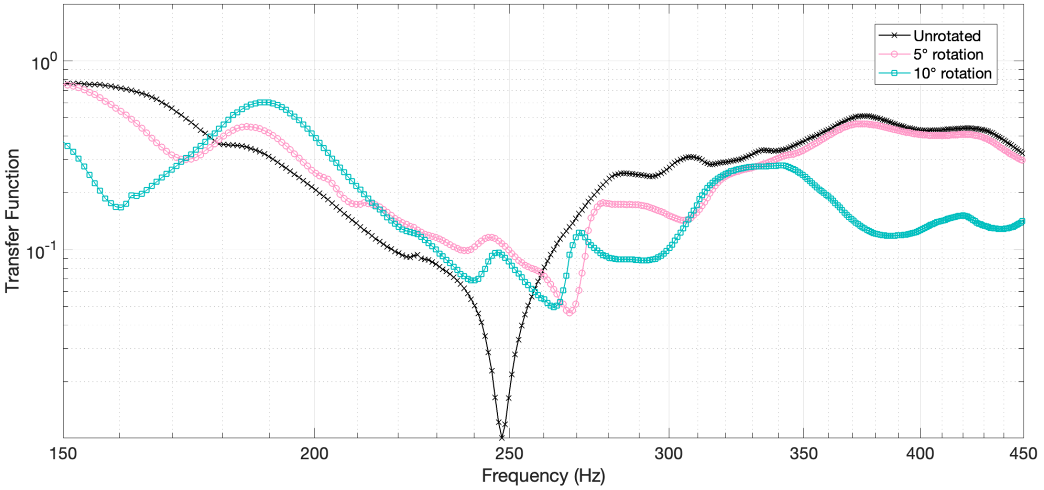

Figure 6.5: Transfer function, for high frequencies, obtained by rotating a sample at different degrees and sending a longitudinal wave through it.

The absence of hysteresis in the samples underscores their reproducibility and reliability, allowing for consistent measurements over time without significant deviations. As depicted in the graph illustrating the response of a sample to various rotation actuations, the absence of hysteresis is evident in the repeated measurements, signifying the material's stable and predictable behavior. This characteristic is crucial for applications requiring precise and repeatable responses to external stimuli, such as tunable metamaterials or adaptive structures.

The reproducibility of measurements enhances the material's utility across a wide range of fields, offering a dependable platform for further research and technological development.

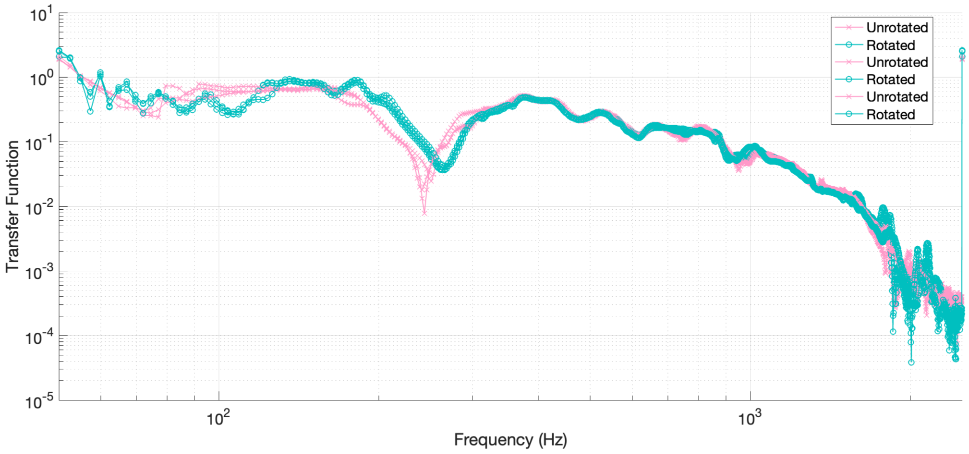

Figure 6.6: Rotate sample forward and backward by same degree to get transfer function.

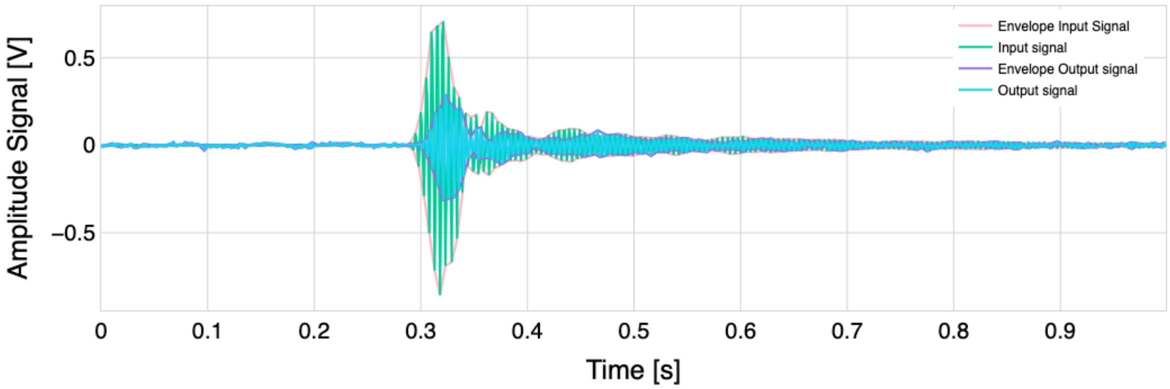

Figure 6.7: Amplitude of the Input and Output signal and their envelope signal in function of time. Measurement performed on sample with drops where the frequency sent in the Gaussian signal is 200 Hz.

Moving on to the second experimental setup involving larger samples, our focus now turns to characterizing the wave dynamics produced by our equipment. Initially, our goal was to identify the nature of the waves generated based on the measured group velocity using our setup. To achieve this, we employed two different types of forcing. First, we stimulated longitudinal waves by striking one end of the sample at its lower center. Second, to excite transverse waves, we positioned one of the clamps at the sample's ends, allowing the vibrator to strike one end of the clamp. These experiments were conducted using a blank sample, providing benchmark values that could be theoretically calculated, as outlined in Annex A.4. In Fig. 6.7 is possible to see an example of measurements performed and used to determined the average group velocities for longitudinal and transverse waves to be 48.95 cm/s and 14.32 cm/s, respectively. Notably, these experimental values, show in Fig. 6.8, matched their theoretical counterparts derived from the material's shear and bulk modulus, highlighting the reliability of our experimental setup and confirming our theoretical framework.

These findings represent a significant congruence between experimental and theoretical results, which underscores the robustness of our methodology and reinforces its usefulness in accurately predicting material properties. This allows us to move on to measuring the group velocities of a sample with fluid inclusions to verify that they modify the speed at which the wave travels through the material.

Figure 6.9 illustrates the outcomes of measuring group velocities for a droplet sample when subjected to a transverse wave. Initially, a baseline measurement was conducted on the sample mounted in the setup without any rotational application. This allowed for the determination of the group velocity for the sample with droplets, yielding an average value of 29.52 cm/s. Remarkably, this velocity significantly surpassed that measured for similar waves in the white material, more than doubling the observed velocity. This could be explained by the alteration in internal structure between the two samples. Modifications to the material's geometry or internal makeup can significantly impact how waves propagate. By reinforcing or rearranging the components within the material, greater coherence and faster wave transmission can be achieved, ultimately resulting in a higher group velocity.

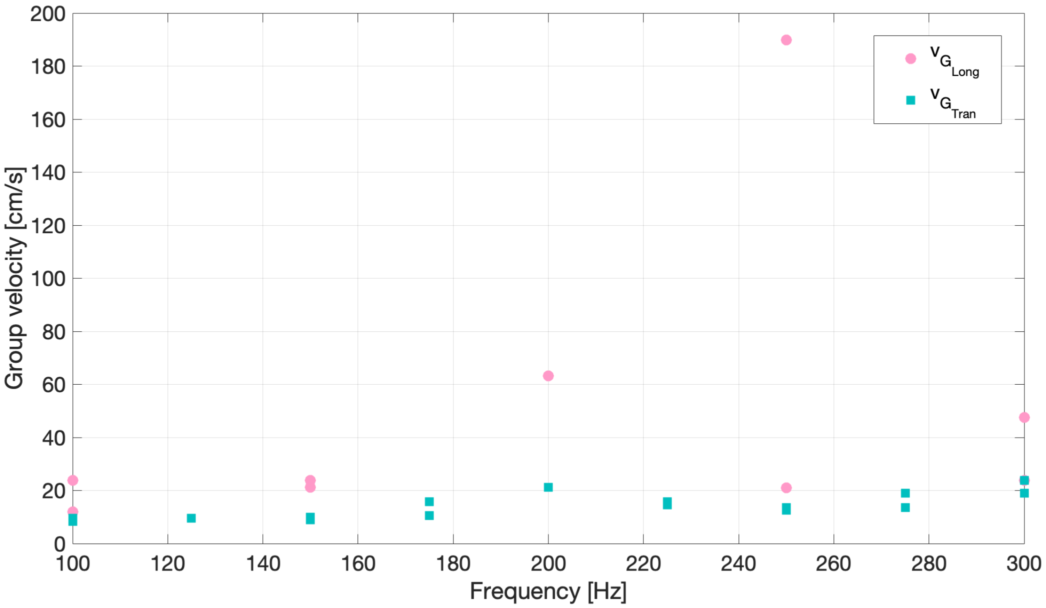

Figure 6.8: Group velocity measure for two types of waves: longitudinal and transverse wave in blank sample.

In the subsequent measurement, we used the same sample and rotated the opposite end of the sent wave by 90°, as illustrated in Figure 6.9. This helicity change impacted the internal structure, resulting in a decrease in the measured group velocity compared to the previous measurement.

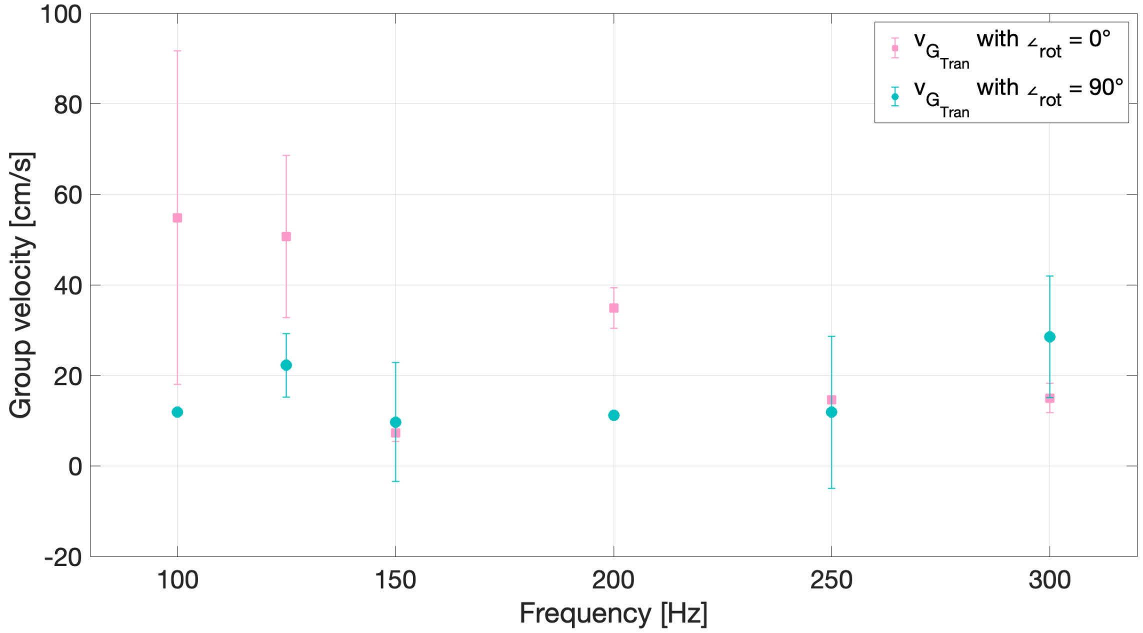

Figure 6.9: Group velocity measure for transverse waves in droplet sample for two different rotation angles: 0º and 90º.

The average value recorded was 15.88 cm/s, indicating that group velocity decreases when the material is rotated due to two possible reasons. Firstly, rotating the material generates additional stress, which can modify the velocity. Secondly, a significant rotation causes the wavelength to increase in size, decreasing frequency and velocity.

6.3.2.2. Compression

The succeeding external actuation method introduced in this study is compression. This section aims to provide additional insights into our materials' actuation capabilities and elucidate how their mechanical response evolves under external compression forces. By exploring the material's behavior under compression, we aim to broaden our understanding of its dynamic properties and establish a comprehensive framework for its potential applications in various fields.

The findings in this section stem from a parallel research endeavor in which I actively participated. This study employs a distinct approach to fabricating mechanical metamaterials, utilizing a layered drop deposition technique, see Annex A.6 7.1. Notably, this methodology shares similarities with our primary research regarding material composition and periodic internal structure. Although the drops in this study consist of water, our analysis focuses primarily on the structural similarities between the two sets of samples. Both studies focus on creating elastic materials with periodic drop structures.

We seek to leverage collective insights to enrich our understanding of mechanical metamaterials by drawing parallels between these distinct yet related research efforts. Despite differences in fabrication techniques and material composition, the shared goal of creating periodic internal structures highlights the universality of certain principles governing their mechanical behavior.

Annex A.6 provides detailed information on the construction and physical characterization of the samples and the experimental procedures applied.

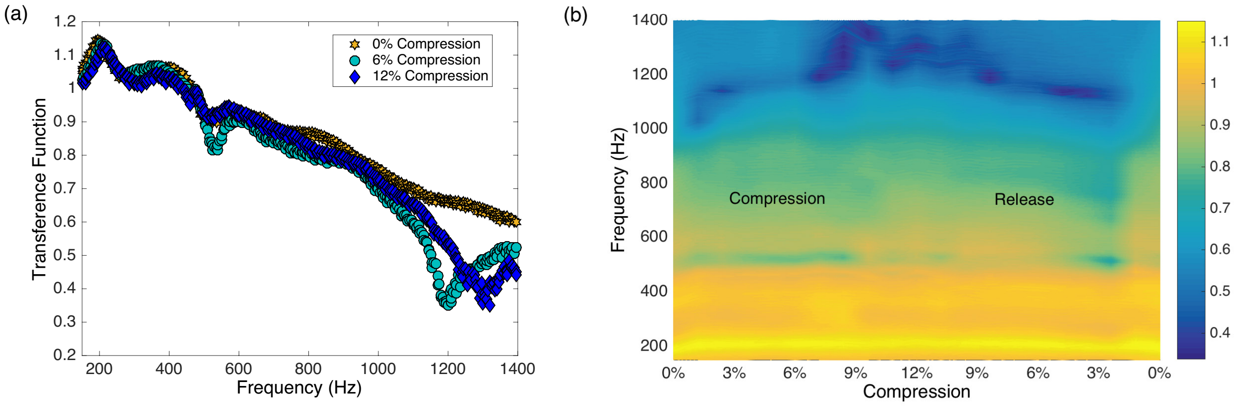

Figure 6.10: (a) Transfer function for the Sample 1 sample for 0% , 6% and 12% compression rates. (b) Transfer function color map for a mechanical metamaterial sample as a function of frequency and compression rates.

In summary, the constructed material is a cube of 55 mm edge, formed by a periodic structure of water droplets inside created by dripping with a modified 3D printer; the radius of the droplets of sample 1 is 2 mm, the XY plane consists of 6x6 droplets separated at 6 mm, this is repeated four times along the Z axis with a separation of 4.5 mm. However, the focal point of interest lies in the results gleaned from the compression process, shedding light on the material's dynamic response under external loading. Compressions were systematically applied to the samples using a mechanical press, enabling the measurement of their mechanical behavior. The measurement protocol employed mirrored the methodology outlined in the earlier discussion on acoustic spectroscopy, wherein a swept sine signal spanning frequencies from 150 to 1400 Hz was utilized.

Figure 6.10 a) illustrates the material's transmission function plotted against frequency for each compression level, revealing patterns similar to previous experiments with rotations. Notably, at a compression level of 6%, distinctive absorption bands emerge around 520 and 1300 Hz. However, as the compression level increases to 12%, these absorption bands undergo modifications in either their intensity or frequency position. This nuanced evolution in the material's transmission function highlights the intricate interplay between compression-induced structural changes and the resulting alterations in wave propagation characteristics.

Figure 6.10 b) presents a heat map depicting the transmission function as a function of compression ratio and subsequent release. This graphical representation offers a comprehensive visualization of absorption bands and enables a more explicit observation of their behavior across different compression levels. Moreover, it serves as a crucial tool for verifying the reversibility of the compression process, as the material demonstrates consistent behavior upon release at the same compression ratios. This reassures the material's stability and reproducibility, underlining its potential for practical applications where reversible and controllable acoustic properties are paramount.

These results effectively showcase the functionality of the metamaterials produced, which exhibit a proportional mechanical response that corresponds with the applied action. It is worth noting that the only discernible difference between this material and the one developed in this thesis is the frequency range at which changes are initiated. The cubic material displays mechanical responses at higher frequencies, surpassing 200 Hz, while our materials exhibit responses at lower frequencies, typically around 50 Hz.

Chapter 7

Conclusions

The construction of elastic mechanical metamaterials, with their tunable characteristics and compliant behavior, has long been a scientific puzzle. However, this thesis unveils a novel approach that successfully created a specialized 3D printer using the Rayleigh-Plateau instability. This innovative method, a fusion of fluid dynamics principles and additive manufacturing, holds the potential to revolutionize the construction of mechanical metamaterials. It opens up exciting new possibilities for designing and fabricating materials with tailored internal structures and mechanical properties, harnessing the inherent instabilities in fluid behavior to design metamaterials with unprecedented characteristics.

Metamaterials can be produced within 15 minutes, with only 10% of that time dedicated to the actual printing process. The remaining time is required for the material to polymerize. The size of the material ranges from 10 to 30 cm, dictated only by the size of the needles employed, while its shape can be modified by the container used. The internal arrangement of needles can also be altered, allowing for multiple configurations. The droplet size featured in this thesis ranges from 1-2 mm in diameter, but this can be adjusted by altering the size of the needle, the flow rate of the material, the printer's speed, and the separation between droplet planes, which is determined by the zig-zag movement. This allows for separate control of the distances established by the Rayleigh-Plateau instability and the abovementioned parameters.

The successful calibration of the printer, establishing a clear correlation between its parameters-vertical velocity, the amplitude of the zig-zag movement, and flux rate injected-and the characteristic distances, droplet size, and separation between them defining the internal structure, is a significant achievement in this research effort. This precision ensures the reproducibility and reliability of the printing process. By meticulously adjusting the printer settings, we have unlocked the ability to precisely control the internal architecture of the printed objects precisely, enabling tailored manipulation of material properties and functionalities.

This study has garnered valuable insights into the dynamic behavior of materials that contain internal periodic fluid distributions. This highlights their remarkable ability to filter mechanical waves at specific frequencies selectively. Our systematic experimentation and analysis have demonstrated that the internal distribution of materials plays a pivotal role in shaping their mechanical response and wave propagation characteristics. Our findings also underscore the sensitivity of wave propagation to various material configurations, emphasizing the importance of considering structural variations in understanding and utilizing wave phenomena.

Also, this work has provided compelling evidence of the actuatable nature of the created materials, showcasing their ability to dynamically respond to external stimuli through two distinct modes of actuation: rotation and compression. A chiral structure was ingeniously engineered by subjecting these materials to rotational forces, highlighting their versatility in achieving tailored material properties. Additionally, through meticulous experimentation and analysis, we have demonstrated how compression serves as another potent mechanism to modify the mechanical response of these materials. These findings underscore the versatility and adaptability of the materials, paving the way for their application in a wide array of fields ranging from advanced materials science to mechanical engineering. As we navigate the frontiers of material design and functionality, the insights gained from this research will undoubtedly catalyze further innovation and exploration, driving the boundaries of what is achievable in actuatable materials.

7.1. Improvements and future work

Looking ahead, the continued exploration and refinement of these methodologies hold the promise of unlocking new advances in materials design. This could pave the way for developing next-generation structures with enhanced functionalities in various applications, marking a significant step forward in materials science and engineering. Some of the proposed improvements and future work include the following:

- To assess the metamaterial's filtering capabilities at a specific frequency comprehensively, it is imperative to meticulously analyze the band structure of the internal configuration through multiple scattering theory. Liu [18] and Chen [19] have executed similar calculations for elastic periodic structures with spherical inclusions. The only variable to consider is that the inclusions are made of viscous fluids instead of solids.

- It is imperative to devise a comprehensive measurement methodology to calculate and effectively validate Oldano and Ponti's findings [16]. The encountered challenge pertains to measuring and characterizing the transverse modes T_1 and T_2. Given the intricacies of forming a chiral structure, a minimum of five accelerometers must be strategically mounted on the sample to facilitate the discrimination and analysis of these modes by the proposed system by the scholars above. Furthermore, it is imperative to conduct resonance ultrasonic spectroscopy to derive precise values for the material constants C_{55} and C_{66}, to have the theoretical values, and to compare them with the measurements to be made.

- One suggestion is to investigate the development of metamaterials utilizing ferrofluid as the injectable fluid. The goal is to create 4D metamaterials, where time serves as the fourth dimension. By incorporating magnetic inclusions, these materials can be influenced by a magnetic field that changes over time, that would generate a change in the response of the material, see details in Annex A.7 7.1.

Bibliography

[1] Katia Bertoldi, Pedro M. Reis, Stephen Willshaw, and Tom Mullin. Negative poisson's ratio behavior induced by an elastic instability. *Advanced Materials*, 22(3):361–366, 2010.

[2] G.C Ma and P. Sheng. Acoustic metamaterials: From local resonances to brad horizons. *Science Advances*, 2(2):e1501595, 2016. doi: 10.1126/sciadv.1501595.

[3] Y.F. Wang, Y.Z. Wang, B. Wu, W.Q. Chan, and Y.S. Wang. Tunable and active phononic crystals and metamaterials. *Applied Mechanics Reviews*, 02 2020. doi: 10.1115/1.4046222.

[4] Nikolay I. Zheludev. The road ahead for metamaterials. *Science*, 328(528), 2010.

[5] E. Barchiesi, M. Spagnuolo, and L. Placidi. Mechanical metamaterials: a state of the art. *Mathematics and Mechanics of Solids*, pages 212–234, 2019. doi: 10.1177/1081286517735695.

[6] Davood Mousanezhad, Sahab Babaee, Hamid Ebrahimi, Ranajay Ghosh, Abdelmagid Salem Hamouda, Katia Bertoldi, and Ashkan Vaziri. Hierarchical honeycomb auxetic metamaterials. *Scientific Reports*, 5:18306, 2015.

[7] S. Singamaneni, K. Bertoldi, S. Chang, J. H. Jang, E. L. Thomas, M. C. Boyce, and V. V. Tsukruk. Bifurcated mechanical behavior of deformed periodic porous solids. *Advanced Functional Materials*, 19:1426–1436, 2009.

[8] Corentin Coulais, Dimitrios Sounas, and Andrea Alù. Static non-reprocity in mechanical metamaterials. *Nature*, 542(7642):461–464, 2017.

[9] B. Grossi, H. Palza, J.C. Zagal, C. Falcón, and G. During. Metarpillar: Soft robotic locomotion based on buckling-driven elastomeric metamaterials. *Materials Design*, 212:110285, 2021. ISSN 0264-1275. doi: https://doi.org/10.1016/j.matdes.2021.110285. URL https://www.sciencedirect.com/science/article/pii/S0264127521008406.

[10] S. Tomotika. On the instability of a cylindrical thread of a viscous liquid surrounded by another viscous fluid. *Proceedings of the Royal Society of London. Series A, Mathematical an Physical Sciences*, 150(870):322–337, 1935.

[11] J.A.F. Plateau. *Statique expérimentale et théorique des liquides soumis aux seules forces moléculaires*. Number v. 2 in Statique expérimentale et théorique des liquides soumis aux seules forces moléculaires. Gauthier-Villars, 1873. URL https://books.google.cl/books?id=l70KAAAAIAAJ.

[12] Lord Rayleigh. On the instability ofiets. *Proceedings of the London Mathematical Society*, 10(4), 1879.

[13] François Gallaire and P.-T. Brun. Fluid dynamic instabilities: theory and application to pattern forming in complex media. *Philosophical Transactions of the Royal Society*

A: Mathematical, Physical and Engineering Sciences, 375(2093):20160155, 2017. doi: 10.1098/rsta.2016.0155. URL https://royalsocietypublishing.org/doi/abs/10.1098/rsta.2016.0155.

[14] D. Brill and G. Gaunaurd. Resonance theory of elastic waves ultrasonically scattered from an elastic sphere. *The Journal of the Acoustical Society of America*, 81(1):1–21, 01 1987. ISSN 0001-4966. doi: 10.1121/1.394983. URL https://doi.org/10.1121/1.394983.

[15] I. E. Psarobas, N. Stefanou, and A. Modinos. Scattering of elastic waves by periodic arrays of spherical bodies. *Physical Review B*, 62(1):278–291, July 2000. ISSN 1095-3795. doi: 10.1103/physrevb.62.278. URL http://dx.doi.org/10.1103/PhysRevB.62.278.

[16] C. Oldano and S. Ponti. Acoustic wave propagation in structurally helical media. *Phys. Rev. E*, 63:011703, Dec 2000. doi: 10.1103/PhysRevE.63.011703. URL https://link.aps.org/doi/10.1103/PhysRevE.63.011703.

[17] Lingzhi Cai, Joel Marthelot, and P.-T Brun. An unbounded approach to microfluidics using the rayleigh-plateau instability of viscous threads directly drawn in a bath. *PNAS Engineering*, 2010.

[18] Zhengyou Liu, C. T. Chan, Ping Sheng, A. L. Goertzen, and J. H. Page. Elastic wave scattering by periodic structures of spherical objects: Theory and experiment. *Phys. Rev. B*, 62:2446–2457, Jul 2000. doi: 10.1103/PhysRevB.62.2446. URL https://link.aps.org/doi/10.1103/PhysRevB.62.2446.

[19] Huanyang Chen, Kin Hung Fung, Hongru Ma, and C. T. Chan. Polarization gaps and negative group velocity in chiral phononic crystals: Layer multiple scattering method. *Phys. Rev. B*, 77:224304, Jun 2008. doi: 10.1103/PhysRevB.77.224304. URL https://link.aps.org/doi/10.1103/PhysRevB.77.224304.

[20] W.M. Jones K. Walters. *Instrumentation Reference Book (Fourth Edition), Chapter 7 - Measurement of Viscosity*. Butterworth-Heinemann, 2010. ISBN 9780750683081. doi: https://doi.org/10.1016/B978-0-7506-8308-1.00007-3.

[21] Mika Latikka, Matilda Backholm, Jaakko V.I. Timonen, and Robin H.A. Ras. Wetting of ferrofluids: Phenomena and control. *Current Opinion in Colloid Interface Science*, 36:118–129, 2018. ISSN 1359-0294. doi: https://doi.org/10.1016/j.cocis.2018.04.003. URL https://www.sciencedirect.com/science/article/pii/S1359029417301449. Wetting and Spreading.

Annexes

Annex A.1

Dispersion relationship of Rayleigh-Plateau instability calculation

```
det1 = ( {
    {x*BesselI[0, x] - BesselI[1, x],
     BesselK[1, x], -x*BesselK[0, x] - BesselK[1, x]},
    {BesselI[0, x] + x*BesselI[1, x], -BesselK[0, x], -BesselK[0, x] +
       x*BesselK[1, x]},
    {(μ/ν)*x*BesselI[0, x], BesselK[1, x], -x*BesselK[0, x]}
   } );
det2 = ( {
    {BesselI[1, x], BesselK[1, x], -x*BesselK[0, x] - BesselK[1, x]},
    {BesselI[0, x], -BesselK[0, x], -BesselK[0, x] +
      x*BesselK[1, x]},
    {(μ/ν)*BesselI[1, x], BesselK[1, x], -x*BesselK[0, x]}
   } );
det3 = ( {
    {BesselI[1, x],
     x*BesselI[0, x] - BesselI[1, x], -x*BesselK[0, x] -
      BesselK[1, x]},
    {BesselI[0, x],
     BesselI[0, x] + x*BesselI[1, x], -BesselK[0, x] +
      x*BesselK[1, x]},
    {(μ/ν)*BesselI[1, x], (μ/ν)*x*BesselI[0, x], -x*
      BesselK[0, x]}
   } );
det4 = ( {
    {BesselI[1, x], x*BesselI[0, x] - BesselI[1, x], BesselK[1, x]},
    {BesselI[0, x], BesselI[0, x] + x*BesselI[1, x], -BesselK[0, x]},
    {(μ/ν)*BesselI[1, x], (μ/ν)*x*BesselI[0, x],
     BesselK[1, x]}
   } );

ENE = BesselI[1, x]*Det[det1] - {x*BesselI[0, x] - BesselI[1, x]}*
    Det[det2];

DE = (μ/ν)*{x*BesselI[0, x] - BesselI[1, x]}*
    Det[det1] - (μ/ν)*{(x^2 + 1)*BesselI[1, x] -
      x*BesselI[0, x]}*Det[det2] - {x*BesselK[0, x] + BesselK[1, x]}*
    Det[det3] - {(x^2 + 1)*BesselK[1, x] + x*BesselK[0, x]}*Det[det4];

phi[x_, μ_, ν_, T_, a_] :=
   ((T*(1 - x^2))/( 2*a*μ))*{1/ν BesselI[1, x] (-x^2 μ BesselI[0, x] BesselK[0, x]^2 +
```

```
        x^2 ν BesselI[0, x] BesselK[0, x]^2 -
        x ν BesselI[1, x] BesselK[0, x]^2 -
        2 x μ BesselI[0, x] BesselK[0, x] BesselK[1, x] +
        x ν BesselI[0, x] BesselK[0, x] BesselK[1,
         x] - ν BesselI[1, x] BesselK[0, x] BesselK[1, x] +
        x^2 μ BesselI[0, x] BesselK[1, x]^2 - ν BesselI[0,
         x] BesselK[1, x]^2 -
        x^2 ν BesselI[0, x] BesselK[1, x]^2) -
      1/ν (x BesselI[0, x] -
        BesselI[1, x]) (-x μ BesselI[1, x] BesselK[0, x]^2 +
        x ν BesselI[1, x] BesselK[0, x]^2 -
        2 μ BesselI[1, x] BesselK[0, x] BesselK[1,
         x] + ν BesselI[1, x] BesselK[0, x] BesselK[1,
         x] - ν BesselI[0, x] BesselK[1, x]^2 +
        x μ BesselI[1, x] BesselK[1, x]^2 -
        x ν BesselI[1, x] BesselK[1, x]^2)}/{-(
       1/ν) (x BesselK[0, x] +
        BesselK[1, x]) (-x^2 μ BesselI[0, x]^2 BesselK[0, x] +
        x^2 ν BesselI[0, x]^2 BesselK[0, x] +
        x μ BesselI[0, x] BesselI[1, x] BesselK[0, x] -
        2 x ν BesselI[0, x] BesselI[1, x] BesselK[0,
         x] + μ BesselI[1, x]^2 BesselK[0, x] +
        x^2 μ BesselI[1, x]^2 BesselK[0, x] -
        x^2 ν BesselI[1, x]^2 BesselK[0, x] -
        x μ BesselI[0, x]^2 BesselK[1, x] + μ BesselI[0,
         x] BesselI[1, x] BesselK[1, x]) -
      1/ν (x BesselK[0, x] + (1 + x^2) BesselK[1,
         x]) (μ BesselI[1, x]^2 BesselK[0, x] +
        x μ BesselI[0, x]^2 BesselK[1, x] -
        x ν BesselI[0, x]^2 BesselK[1, x] - μ BesselI[0,
         x] BesselI[1, x] BesselK[1, x] +
        2 ν BesselI[0, x] BesselI[1, x] BesselK[1, x] -
        x μ BesselI[1, x]^2 BesselK[1, x] +
        x ν BesselI[1, x]^2 BesselK[1, x]) +
      1/ν^2 μ (x BesselI[0, x] -
        BesselI[1, x]) (-x^2 μ BesselI[0, x] BesselK[0, x]^2 +
        x^2 ν BesselI[0, x] BesselK[0, x]^2 -
        x ν BesselI[1, x] BesselK[0, x]^2 -
        2 x μ BesselI[0, x] BesselK[0, x] BesselK[1, x] +
        x ν BesselI[0, x] BesselK[0, x] BesselK[1,
         x] - ν BesselI[1, x] BesselK[0, x] BesselK[1, x] +
        x^2 μ BesselI[0, x] BesselK[1, x]^2 - ν BesselI[0,
         x] BesselK[1, x]^2 -
        x^2 ν BesselI[0, x] BesselK[1, x]^2) -
      1/ν^2 μ (-x BesselI[0, x] + (1 + x^2) BesselI[1,
         x]) (-x μ BesselI[1, x] BesselK[0, x]^2 +
        x ν BesselI[1, x] BesselK[0, x]^2 -
        2 μ BesselI[1, x] BesselK[0, x] BesselK[1,
         x] + ν BesselI[1, x] BesselK[0, x] BesselK[1,
         x] - ν BesselI[0, x] BesselK[1, x]^2 +
        x μ BesselI[1, x] BesselK[1, x]^2 -
        x ν BesselI[1, x] BesselK[1, x]^2)};
```

Annex A.2

Rheology of Vinyl Polysiloxane

Given the need to know the viscosity of the chosen elastomer with certainty, it was decided to carry out a rheology study to calculate the dispersion ratio of our experimental setup.

Rheology is the study of deformation and flow deformation, specifically in systems whose behavior is poorly defined, meaning the area between elastic solids and perfectly viscous fluids. These materials are called viscoelastic because they can not be characterized only in terms of one variable; in this case, just elastic modulus or material viscosity; it is a mix between both features.

In our case, the fluid under study was vinyl polysiloxane (VPS), and it was necessary to know how its viscosity behaves due to its cross-linking properties. The study used a strain-controlled rheometer, where the known deformation applied was shear-rate, and its geometry was a cone-and-plate one.

A simple explanation of how this type of rheometer works is the following: given a rheometer geometry, the sample is placed between the two plates, and if applied, some influential parameters on the behavior of the fluid in question need to be adjusted, such as temperature and test range, after setting all the parameters, one of the plates starts to move while the other remains stationary measuring the shear stress that the fluids are receiving, with this measure, the viscosity can be obtained.

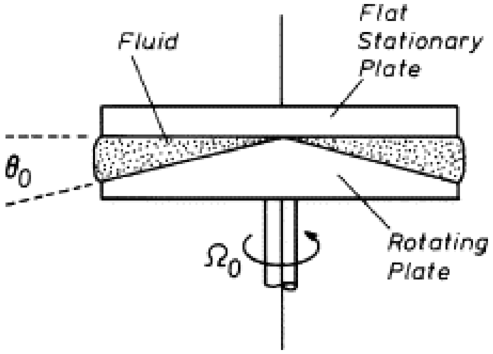

Figure 7.1: Schematic of cone-plate flow of a fluid, where the flat plate is stationary and the cone rotates with an angular velocity Ω_0[20]

As can be seen in the Fig. 7.2, the viscosity of the elastomers remains almost constant, $\nu = 2.07 \pm 0.17$ [Pa s], over some time, that time is significant, as it provides the time frame we have available to work with for printing our 3D metamaterial sample.

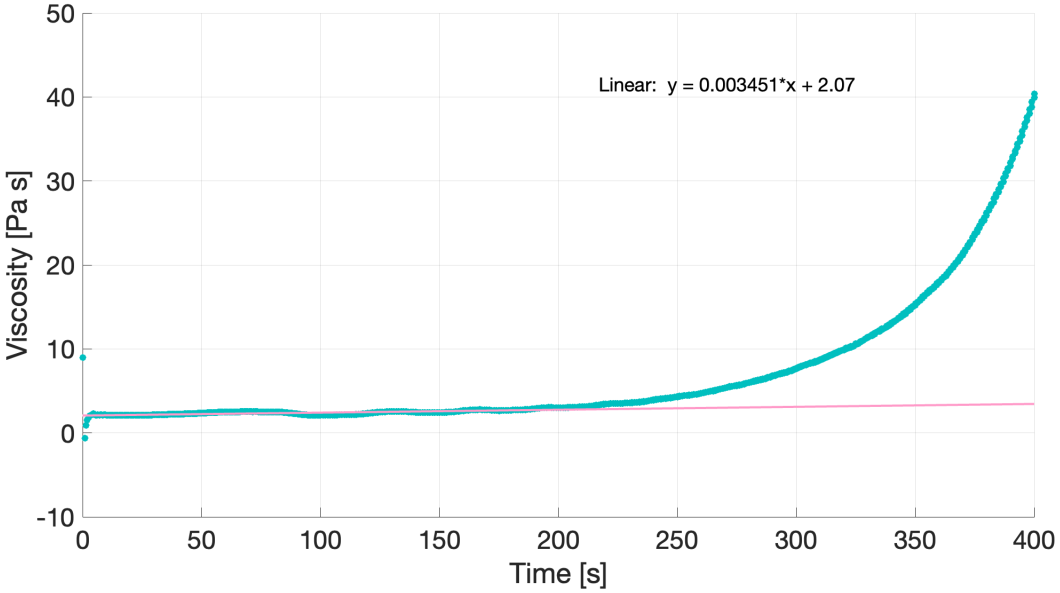

Figure 7.2: Rheologhy study made for vinyl polisiloxane Zhermack Elite Double 22 Fast at 23ºC

Annex A.3

Printer program code

```
#include <Arduino.h>
#include <LiquidCrystal_I2C.h>
#include <Keypad.h>
#include <Stepper.h>


int lcdCols = 16;
int lcdRows = 2;

LiquidCrystal_I2C lcd;


TaskHandle_t AxisXcodeTask;
TaskHandle_t AxisYcodeTask;


#define IN1 4
#define IN2 16

#define IN3 15
#define IN4 2


const int stepsPerRevolution_X = 1000;
const int stepsPerRevolution_Y = 1000;


const int stepsX = 1000;
const int stepsY = 1000;



Stepper axisX(stepsPerRevolution_X, IN1, IN2);
Stepper axisY(stepsPerRevolution_Y, IN3, IN4);



const byte ROWS = 4;
const byte COLS = 4;
char keys[ROWS][COLS] = {
  {’1’,’2’,’3’,’A’},
  {’4’,’5’,’6’,’B’},
  {’7’,’8’,’9’,’C’},
  {’*’,’0’,’#’,’D’}
};


uint8_t rowPins[COLS] = {13, 12, 14, 27};
uint8_t colPins[ROWS] = {26, 25,33, 32};


```

```
Keypad keypad = Keypad( makeKeymap(keys), colPins, rowPins, ROWS, COLS );


enum state {WAITING, LOOPING};
state current_state = WAITING;


const char EXITKEY = ’A’;


void keypadEvent(KeypadEvent key){
  switch(keypad.getState()){
    case PRESSED:
      switch(key){
        case ’A’:
          lcd.clear();
          lcd.print("Crescente");
          current_state = WAITING;
          break;
        case ’C’:
          lcd.clear();
          lcd.setCursor(4,1);
          lcd.print("printing");
          current_state = LOOPING;
          break;
      }
      break;
  }
}


void forward(Stepper Axis, int steps){
  Axis.step(steps);
  return;
}


void backward(Stepper Axis, int steps){
  Axis.step(-steps);
  return;
}


void X_loop(Stepper axis, int stepsX){

    forward(axis, 8 * stepsX);
    delay(3);
    backward(axis, 8 * stepsX);
    delay(3);

}

void AxisXcode(void * parameter){
  for(;;){
    char key = keypad.getKey();

```

```
  switch(current_state){
    case WAITING:

      if (key == ’4’){
        lcd.clear();
        lcd.setCursor(0,0);
        lcd.print("Forward");
        lcd.setCursor(0,1);
        lcd.print("4000 steps");
        forward(axisX, 4000);
      }
      if (key == ’7’){
        lcd.clear();
        lcd.setCursor(0,0);
        lcd.println("Backward");
        lcd.setCursor(0,1);
        lcd.println("4000 steps");
        backward(axisX, 4000);

      }
      break;
    case LOOPING:
      X_loop(axisX, stepsX);
      break;
  }
 }
}


void Y_loop(Stepper axis, int stepsY){
  forward(axis,stepsY);
}


void setup(){

  axisX.setSpeed(2000);
  axisY.setSpeed(1000);
  keypad.addEventListener(keypadEvent);


  lcd.begin(16,2);
  lcd.clear();
  lcd.backlight();
  lcd.println("Crescente");
  delay(2000);

  xTaskCreatePinnedToCore(
    AxisXcode,
    "AxisXcode",
    10000,
    NULL,
    1,
    &AxisXcodeTask,
    1);
}
```

```


void loop(){
  char key = keypad.getKey();

    switch(current_state){
        case WAITING:

            if (key == ’5’){
                lcd.clear();
                lcd.setCursor(0,0);
                lcd.print("Up");
                lcd.setCursor(0,1);
                lcd.print("4000 steps");
                forward(axisY, 4000);

            }
            if (key == ’8’){
                lcd.clear();
                lcd.setCursor(0,0);
                lcd.print("Down");
                lcd.setCursor(0,1);
                lcd.print("4000 steps");
                backward(axisY, 4000);
            }
            break;
        case LOOPING:
            Y_loop(axisY, stepsY);

            break;
    }

}
```

Annex A.4

Theoretical approximation for the bandgap and calculation of material constants

Shear Modulus G and Bulk Modulus K

Using a compression study performed by a Mechanical Engineering student of our University, we will calculate the shear modulus and compressibility from the experimental results obtained for Young's modulus, E, and Poisson's Coefficient, ν:

$$E = 440kPa \qquad \nu = 0.47$$

Thus the shear modulus and bulk modulus can be expressed in terms of Young's modulus (E), Poisson's ratio (ν), and density (ρ) for isotropic materials. These expressions are as follows:

$$G = \frac{E}{2(1+\nu)}$$

$$K = \frac{E}{3(1-2\nu)}$$

By replacing the values of the study and considering that the density of the polymer is $\rho_{VPS} = 1112.1kg/m^3$, the following values are obtained:

$$G = 149kPa \qquad K = 2444kPa$$

Group velocity for longitudinal waves, v_{Gl},and transversal waves, v_{Gt}

The velocity of a longitudinal wave (v_{Gl}) and a transverse wave (v_{Gt}) can be expressed in terms of various elastic constants and material properties for an isotropic material. Here are the expressions:

- Velocity of longitudinal wave: $v_{Gl} = \sqrt{\frac{K+\frac{4}{3}G}{\rho}}$
- Velocity of transversal wave: $v_{Gt} = \sqrt{\frac{G}{\rho}}$

By replacing the values of all the constants for the ones calculated before, it obtains the following values for the velocities in the polymer:

$$v_{Gl} = 48.75m/s \qquad v_{Gt} = 11.6m/s$$

Annex A.5

Proceedings presented to 16th International Congress on Artificial Materials for Novel Wave Phenomena - Metamaterials 2022

16^{th} International Congress on Artificial Materials for Novel Wave Phenomena - Metamaterials 2022
Siena, Italy, Sep. 12^{th} - 17^{th} 2022

2022 Sixteenth International Congress on Artificial Materials for Novel Wave Phenomena (Metamaterials) | 978-1-6654-6584-7/22/$31.00 ©2022 IEEE | DOI: 10.1109/METAMATERIALS54993.2022.9920745

Printing tunable mechanical metamaterials using the Rayleigh-Plateau instability

C. Contreras[1,*], **C. Espinoza**[1,2], **C. Falcón**[1]

[1]Universidad de Chile, Departamento de Física, Facultad de Ciencias Físicas y Matemáticas, Beauchef 850, 8370448, Santiago, Chile
[2]Universidad de Chile, Departamento de Sonido, Facultad de Artes, Compañía 1264, 8340380, Santiago, Chile
e-mail: c.contreras.5@ug.uchile.cl

***Abstract* – In the last few years, the study and interest on metamaterials has increase significantly, including a keen focus on their manufacturing. In our work we present a way to harness the well-known Rayleigh-Plateau instability of multiple fluid threads placed within a curing elastomer solution to rapidly manufacture elastic mechanical metamaterials. This method allows the positioning of spherical inclusions of a fluid periodically within an elastic matrix and, thereby, control the dispersion of elastic waves in a periodic medium by only changing a small set of control parameters.**

I. INTRODUCTION

During the last decades, the scientific community has focused their interest into the experimental, theoretical and numerical study of metamaterials and specifically mechanical ones, whose non trivial microscopic structure gives them exotic or unusual mechanical properties [1, 2, 4]. The growing interest has pushed scientist to create methods [6] to classify and sort their counter-intuitive mechanical properties such as auxeticity (negative Poisson's ratio), strain stiffening, or non-reciprocal responses [3]. Due to these unusual properties and possible applications, the study of mechanical metamaterials has become a very interesting research area. In order to test these properties mechanically, it is necessary to build samples systematically and quickly. For that purpose, we develop a new way of printing these materials by making use of the Rayleigh-Plateau instability in polymeric suspensions that cross-link and thus solidify. The new printing method allow spherical inclusions of a fluid to be placed periodically within an elastic matrix (once the polymer suspension is cross-linked) and, thereby, control the dispersion of elastic waves in a periodic medium, particularly when the material forming the inclusion is a fluid or elastic solid. In this context, a new study is added, the case in which the inclusion (both its content an its form) can be controlled externally, changing the dispersion of the elastic waves. This can be achieved by global compression or extension of the sample or by local actuation on the inclusion properties (for instance if the inclusion is made of a ferrofluid liquid which can be controlled by a constant external magnetic field).

II. RALEIGH-PLATEAU INSTABILITY

The operation of the printer is based on the use of Rayleigh-Plateau instability: a cylindrical fluid thread (glycerine) surrounded by another fluid (vynil polysiloxane Elite Double 22 from Zhermack) destabilizes into periodically separated drops by capillary action. Tomotika [5] calculated, in the non-inertial highly viscous limit, the growth rate n of the instability as

$$in = \frac{T}{2a\mu_{out}}(1 - k^2a^2)\phi(ka, \frac{\nu_{in}}{\nu_{out}}), \qquad (1)$$

with T interfacial tension coefficient between both fluids ($\sim$ 10 mN/m), k the modulus of the most unstable wave vector of the spatial disturbance along the thread ($\sim$ 1 cm), a the radius of the initial thread ($\sim$ 1 mm)and (ν_{in}, ν_{out}) the kinematic viscosity of the fluids inside and outside the thread, respectively ($\sim$ 1 Pa s). $\phi(\cdot, \cdot)$ is a dimensionless function of ka and ν_{in}/ν_{out} [5]. With this principle we can design the structure of a mechanical metamaterial by injecting different thread of viscous fluids into a container filled with a cross-linking polymer suspension whose

978-1-6654-6584-7/22/$31.00 ©2022 IEEE

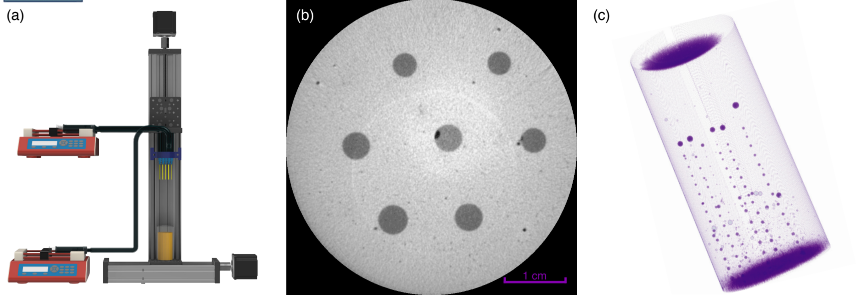

Fig. 1: (a) Experimental setup of 3D mechanical metamaterials printer based on Rayleigh-Plateau instability. (b) Azimuthal tomography slice of a sample showing the hexagonal array of needles. (c) 3D tomography reconstruction of sample #19, $Q = 0.0033cm^3/s$, $v = 0.457cm/s$ and $A = 4mm$.

cross-linking time τ is similar to the time of the instability, allowing us to control the internal structure of the metamaterial (droplet size and wavelength). In this way, multiple threads are injected simultaneously, allowing control of the three-dimensional structure of the constructed mechanical metamaterial. To position these threads inside a container of curing elastomer solution, we built a custom 3D printer, as shown in Fig. 1 (a). A PLA printing head holds an hexagonal array of 7 1.32 mm in diameter 10 cm long steel needles. The distance between each needle is 1.35 cm. Through each needle, a controlled flow Q of printing fluid (glycerin) is injected using syringe pumps (NE-1600 and NE-1000 from New Era pumps). The entire head is mounted on a 1-meter linear vertical stage driven by a stepper motor via an Arduino 1 microprocessor, which allows to control the deposition velocity of the thread v. At the base of the vertical linear stage, a horizontal oscillating one driven by another stepper motor via the same microprocessor as above moves the container in a zig-zag manner with amplitude A and frequency f, which allows to set the position of droplets for the whole array of destabilizing threads [8]. The control parameters of our printer are Q, v, A, τ and f, which set the mechanical properties of the metamaterial sample as they allow the precise deposition of droplets of a given size at a given position. The positioning of these droplets within the cured elastic elastomer matrix is measured using computerized 3D microtomographies (SkyScan 1278 from Bruker). A typical tomographic image of a sample after curing is shown in Fig. 1(c) where colors are chosen arbitrarily. The control of droplet size and locations can be assessed in Fig. 2), where we display the measured diameter of droplets versus the theoretically computed ones as a function of A (a) and of v (b).

III. ACOUSTIC SAMPLE CHARACTERIZATION

The printed elastic samples with the periodically deposited fluid drops are mechanically probed by acoustic spectroscopy. The sweep sine signal from a spectrum analyzer (Stanford SR780 from SRS) amplified by a power audio amplifier (XGA 500 from Gemini) drives an electromechanical shaker (4810 from B&K) attached to one side of the sample. Two micro accelerometers (356A14 from PCB) are positioned on two opposite sides of the sample, one acquiring the excitation signal $e(t)$ and another acquiring the response of the metamaterial $r(t)$. The power spectra of both signals $\hat{e}(f)$ and $\hat{r}(f)$ are computed by the spectrum analyzer, and the transfer function $T(f) = |\hat{r}(f)|/\hat{e}(f)$ is calculated. The possibility of rapidly printing elastic samples with controlled transfer functions for wave propagation is displayed in Fig. 2(c), where band stops appear at given frequencies which are controlled by both droplet size and positioning. A further step on the prediction the mechanic metamaterial's band structure for mechanical waves and the possible actuation is a work in progress.

IV. CONCLUSION

We have deviced a simple way to design and print mechanical metamaterials for wave propagation control by harnessing the Rayleigh-Plateau instability. To do so, we have constructed a 3D printer that injects multiple fluid

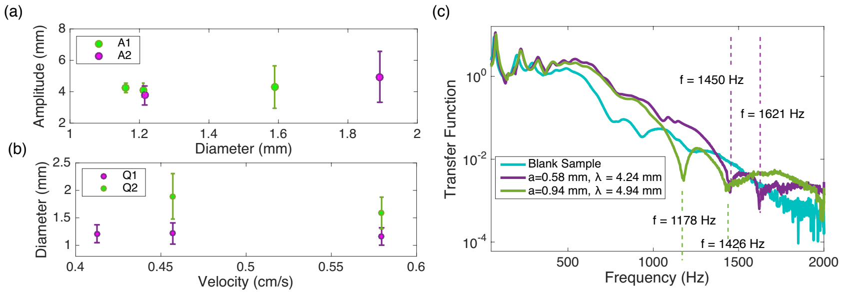

Fig. 2: Characterization of sample with parameters $Q_1 = 0.0033$ cm^3/s, $Q_2 = 0.0083$ cm^3/s, $A_1 = 4$ mm and $A_2 = 2.5$ mm. (a) Wavelength for each sample group at the same forcing amplitude. (b) Drop diameter for each sample group with the same injected flow rate. (c) Taking into account the structural characterization, we decided to compare the frequency response of two different samples and a blank one. We can observe the presence of two absorption bands in the sample with smaller droplet size and wavelength (purple line), which appear to move to the left as the size and wavelength goes larger (green line).

threads within a curing elastomer solution and sets the periodicity of the Rayleigh-Plateau instability via horizontal shearing. From acoustic spectroscopic probing, we have found that the frequency response depends on the diameter and wavelength of the droplets of the metamaterial.

ACKNOWLEDGEMENT

The authors acknowledge the technical support of the Bio-CT Experimental Platform via Fondequip Grant EQM150010. This work was partially supported by FONDECYT Regular Grant #1190005 and FONDECYT Postdoctoral Grant #3200239.

REFERENCES

[1] Ma, G.C., and Sheng, P. (2016).“Acoustic metamaterials: From local resonances to broad horizons”, *Science Advances*, **2**, 1501595.
[2] K. Bertoldi, V. Vitelli, J. Christensen, and M van Hecke (2017).“Flexible mechanical metamaterials”. *Nature Reviews Materials,* **2**, 17066
[3] Barchiesi, E., Spagnuolo, M., Placidi, L. (2019).“Mechanical metamaterials: a state of the art”, *Mathematics and Mechanics of Solids*, **24**, 212-234.
[4] Y. F. Wang, Y. Z. Wang, B. Wu, W. Q. Chen, and Y. S. Wang (2020). “Tunable and Active Phononic Crystals and Metamaterials”. *Applied Mechanics Reviews,* **72**, 040801.
[5] Tomotika S., “On the instability of a cylindrical thread of a viscous liquid surrounded by another viscous fluid”, *Proceedings of the Royal Society of London. Series A, Mathematical an Physical Sciences*, vol. 150, 870, p. 322-337, 1935.
[6] Nicholay I. Zheludev,“The Road Ahead for Metamaterials”, *Science*, vol. 328, 528, 2010.
[7] Katia Bertoldi, Pedro M. Reis, Stephen Willshaw and Tom Mullin, “Negative Poisson’s Ratio Behavior Induced by an Elastic Instability”,*Advanced Materials*, vol. 22, 3, p. 361-366, 2010.
[8] Lingzhi Cai, Joel Marthelot and P-T. Brun, “An unbounded approach to microfluidics using the Rayleigh-Plateau instability of viscous threads directly drawn in a bath.”, PNAS Engineering, 2010.

Annex A.6

Paper submitted to Journal of Manufacturing Processes

Article

Rapid manufacturing of tunable soft elastic metamaterials via droplet deposition in curing elastomeric layers

Fernanda Blanc[1,*], Consuelo Contreras[1], Carolina Espinoza[1,2], Claudio Falcón[1]

[1] Departamento de Física, Facultad de Ciencias Físicas y Matemáticas, Universidad de Chile, Avenida Blanco Encalada 2008, Santiago, Chile
[2] Departamento de Sonido, Facultad de Artes, Universidad de Chile, Compañía de Jesús 1264, Santiago, Chile
* Correspondence: fernanda.blanc@uchile.cl

Version March 15, 2024 submitted to Journal of Manufacturing Processes

Abstract: A rapid manufacturing scheme for soft tunable elastic metamaterials is presented. This scheme is based on the controlled deposition of liquid droplets on curing elastomer layers, forming designed periodic droplet structures in elastomer blocks. A modified 3D printer allows the deposition of printing fluids of different viscosities, such as glycerine and water. As a result, a soft mechanical metamaterial is obtained, with tunable transmission properties verified by acoustic characterization. This technique opens new avenues for rapid prototyping of mechanical metamaterials with desired band-gaps and even 4D printing.

Rapid prototyping of tunable soft elastic metamaterials

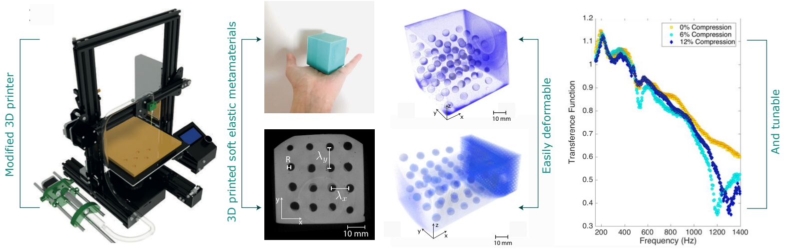

1. Introduction

The design and study of artificially constructed composites has become an important research subject due to capacity to tune and control mechanical responses, in particular wave propagation, endowing theses new materials with unsual or non-trivial mechanical properties. In this sense, they are called mechanical metamaterials [1–4]. Their ability to control wave propagation has a plethora of applications ranging from mechanical cloaking [5–7], to wave guiding [8–11] to noise reduction and absorption [12–14], to mention a few. One of the main issues allowing a proper experimental characterization of mechanical metamaterials and their surprising properties is the sample prototyping process. Additive manufacturing techniques, including laser cutting, soft lithography, two-component fast mold casting and 3D printing (see Ref. [15] and references therein) have been decisive in the advancement of mechanical metamaterial construction and implementation. As these techniques develop and new ones appear (such as two-photon lithography and 3D bioprinting), the range of base materials which can be printed becomes larger and larger, the ways to device samples becomes quicker and quicker and the interface between sample design and sample probing become smoother and smoother, specially in the domain of soft matter [16,17].

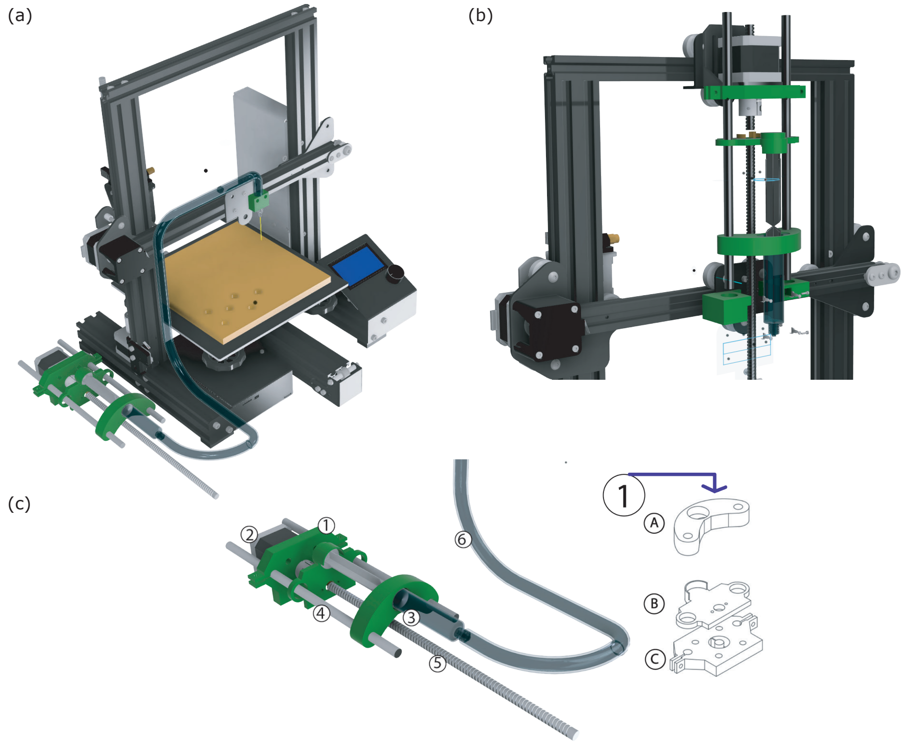

Figure 1. Syringe pump extruder configuration based on Crealty Ender 3 3D printer for (a) high viscosity fluids, and (b) low-viscosity fluids. (c) Syringe pump extruder elements.

One avenue that has become very interesting to pursue is the possible combination of manufacturing techniques to mix fluids solids (plastic, elastic or both), which can lead to different and unexplored classes of mechanical metamaterials and composites [18–20]. In the case where periodic printing of different materials can be positioned inside a matrix of another material, one could easily envision the possibility of on-demand band gaps for mechanical and/or acoustical vibrations along a metamaterial sample. Furthermore, if the matrix, the printing material or both can be externally actuated via a simple operation (such as compression or extension), then the metamaterial's band structure can be tunable. This tunability has been used to generate elastic metamaterials with a broad-band transmission spectrum [21,22] and designed band gaps [23–27], which can be harnessed for several applications in different frequency ranges.

In this work, we present a rapid manufacturing scheme for soft elastic mechanical metamaterials with tunable band gaps which is based on the combination of fast mold casting and 3D printing via droplet deposition [28,29]. The speed and accuracy of the prototyping method allows to generate samples of periodically deposited fluid droplets within an elastomer matrix, which endows the sample with bandgaps. These bandgaps can be readily changed by extension or compression of the elastomer matrix, allowing a simple, direct and reversible control of the transmission properties of the metamaterial. The paper is divided as follows. In Section 2 we present our modified 3D printer, the printing technique and the sample description. Section 3 we describe the tomographic and acoustic characterization procedures of the printed samples, which display tunable band gaps. Finally we discuss our results and conclude on Section 4.

2. Sample construction and printing

2.1. Modified 3D printer

To be able to print high viscosity fluids, such as silicone (VPS), and deposit low viscosity fluids, such as water, we started by modifying a Crealty Ender 3 3D printer [30]. In Fig. 1, there are the two configurations of the position of the syringe pump extruder according to the fluid to be used for extruding: Fig. 1 (a) for low viscosity fluids and Fig. 1 (b) for high viscosity fluids. The main considerations to choose one or another are the ease with which the fluid can flow through the silicone hose, the ability of the syringe to hold the fluid without dripping in the vertical position, and drip flow stabilization.

In Fig. 1 (c) each element of the extruder is signed in a horizontal position as in figure (a), because the only difference with respect to (b) are the couplings through the extruder carriage in the X axis of the printer and an additional cart without straps on the top support to support the weight of the pump itself. On this extruder ① corresponds to the structure printed in PLA+, composed of 3 pieces: Ⓐ is the element that keeps the syringe tube and the linear axes fixed, since it was calculated for that the pieces enter under pressure. On the other hand Ⓑ is the piece that allows to transmit the movement, having the plunger of the syringe stuck in the upper socket, the nut inserted in the lower hole through which the spindle will circulate, and the linear axes at both ends allowing the axes to slide smoothly. When the motor rotates, this part will move linearly pushing or retracting the syringe plunger. By last Ⓒ is the piece that keeps the motor fixed by means of 4 M3 screws placed in the 4 symmetrical holes. The metal coupling that connects the motor with the spindle will pass through the center and the linear axes will be placed at the ends with a reinforcement of 2 Sample 2 screws to keep them fixed. ② corresponds to the NEMA17 stepper motor, which will be connected to the board. This motor is connected by a metal coupling to the spindle ⑤. The number ③ represents the 10 ml plastic syringe, while ④ represents the linear axes with their respective bearings. ⑥ represents the urethane hose, through which the fluid that will go to the needle in the coupling for it in ⑦ will circulate. The coupling is screwed to the extruder carriage of the printer ⑧, and ⑨ corresponds to the VPS material being printed.

Specifically, a PLA+ structure designed in Fusion 360 and sliced by Ultimaker Cura 3D printing software on the original Ender 3 printer was designed for the extruder, along with shafts and linear bearings, and a spindle system with nut and thread, which made it possible to transform the circular movement of the motor into a linear one and thus push the plunger of the syringe, pumping fluid with great precision. The fluid is pushed by a urethane hose connected between the tip of the syringe and a blunt needle, which is fixed by means of a $PLA+$ support in the same place where the conventional nozzle of the printer is placed, thus achieving a control analogous to the original Ender 3 in terms of programming and simplifying distance calculations. The complete system is depicted in figure 2(b), where ⑦ is the printer coupler along with the blunt syringe, ⑧ corresponds to the 3D printer and ⑨ is the VPS under printing process.

2.2. Mechanical metamaterial samples

The manufacturing process of the mechanical metamaterial samples is as follows: first, a mold is printed in PLA+ with the inner dimensions L_x, L_y, L_z, which will be filled with two-part rapidly curing silicone solution (VPS Elite Double 22 Fast from Zhermack), as displayed in Fig. 2 a. The curing time of this silicone solution is shorter than 5 minutes. A silicone layer of height h is deposited within the container. Before it cures, water droplets are deposited on the printing plane. After the layer is cured, a new layer of curing elastomer solution is applied (Fig. 2 b). Repeating this process enable us to control different parameters of the soft mechanical metamaterial. The separation of the droops in the X, Y and Z directions, λ_x, λ_y and $\lambda_z = h$ respectively (Fig. 2 b and c), and the radius R of the drops by changing the needle diameter. The only restriction in determining the droplet separation parameters is the step allowed by the motors.

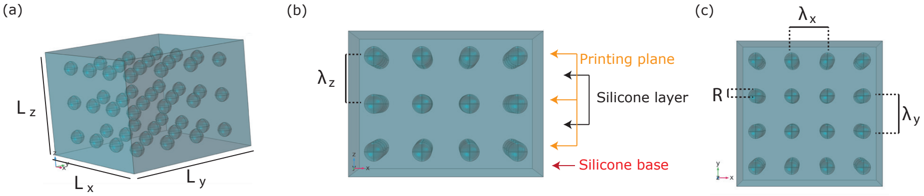

Figure 2. Schematic of mechanical metamaterials fabricated (a) 3D view. $L_{x,y,z}$ are the elastomeric block dimensions (b) XZ view. Silicone base, silicone layers and printing planes. λ_z is the separation between printing planes. (c) XY view. R is the drop radius controlled by the needle diameter, and $\lambda_{x,y}$ are the drop separations.

Sample	R (mm)	$\lambda_{x,y}$ (mm)	λ_z (mm)	$ND_{x,y}$	ND_z
Sample 1	2	6	4.5	6	4
Sample 2	2	8	5	5	5

Table 1. Experimental parameters for metamaterial samples printed using our modified 3D sample.

3. Experimental characterization

3.1. Computarized microtomography

The volume was set at 55×55×55 mm^3 for each sample. While the external dimensions of the sample can be assessed by simple inspection, the internal structure of the printed elastic metamaterial cannot be observed by the naked eye as our VPS solution is opaque, as shown in Figure 3 (a). To allow a direct characterization of the droplet deposition pattern and structure within the cured elastomer matrix, the internal structure of the printed samples was probed via non-intrusive high resolution computarized tomograhy (Micro-CT Skyscan 1278 by Bruker). Each sample was scanned with a 50 μm resolution in Z and 100 μm in X and Y axes. Figure 3 shows the external and internal view of a elastomeric block with water drops fabricated with our technique. From these data we can extract the experimental values of λ_x, λ_y and λ_z, and R, which are found to be within less than 5% of the theoretically predicted values and the ones measured on the surface of the curing elastomer layer. Due to the compliant nature of the elastomer matrix, the internal structure of the drople array can be altered by simple comprresion and/or dilation of the sample. To wit, we constructed a PLA+ press that could fit inside the 80×80×200 mm^3 volume of the Micro-CT sample charriot, allowing us to observed both the relaxed elastomer sample (c.f. Figure 3 (c)) and the effect of a fixed compression on the metamaterial sample internal arrangement (c.f. Figure 3 (d). Colors for the micro-CT images are chosen arbitrarily. From these images, we have checked that the positioning of the droplets in a periodic mesh has an error comparable with the precision of the stepper motors of our modified 3D printer.

3.2. Acoustic spectroscopy

In order to obtain their frequency response, the mechanical metamaterial samples are compressed along their Z axis at rates from 0% up to 12% of their original dimension, while a mechanical excitation is performed using the experimental setup depicted in figure 4. A spectrum analyzer (SR780 from SRS)

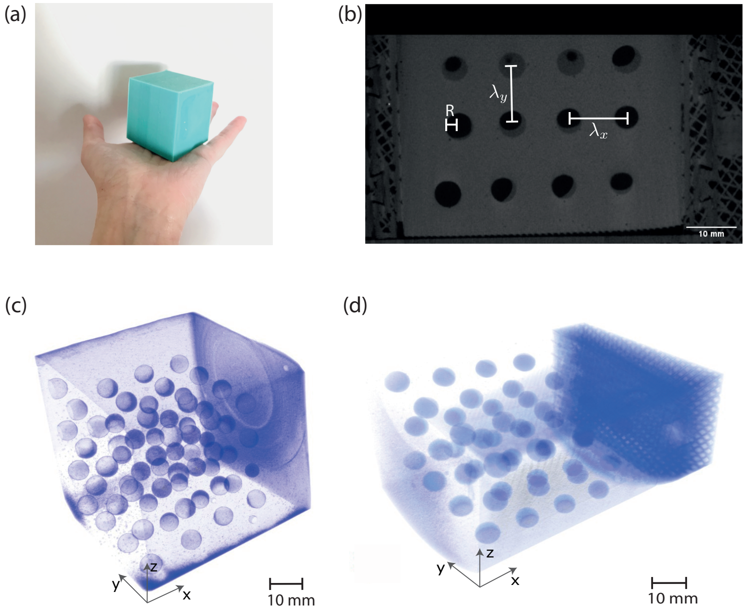

Figure 3. (a) Typical sample size and shaoe. (b) Computarized tomographic image slice in the X-Y plane, showcasing λ_x, λ_y and the radius R of the droplets. (c) Compuratized tomography of the sample showcasing the periodic structure within the elastomer matrix. (d) Compuratized tomography of the compressed sample along the Y axis showcasing the deformation of the periodic structure within the elastomer matrix.

sends a sweep sine signal in a frequency f range $f = [150, 1400]$ Hz with constant amplitude. The signal is amplified by a power audio amplifier (XGA 500 from Gemini) which drives an electro-mechanic shaker (4810 from B&K) exciting the sample. Two micro accelerometers (352C22 from PCB) are conditioned by separatedly by signal conditioners (PCB 408E09) and positioned on two opposite sides of the sample which are not in contact with the mechanical press, one acquiring the excitation signal $e(t)$ and another acquiring the response of the metamaterial $r(t)$. Both accelerometers are attached to the sample during acoustical tests using a couplant gel (Olympus SWC-2). The power spectra of both signals $\hat{e}(f)$ and $\hat{r}(f)$ are computed by the spectrum analyzer, and the transfer function $T(f) = |\hat{r}(f)|/\hat{e}(f)$ is calculated. The specimen is compressed in certain percentage by a mechanical press and the measurement is repeated. A Mitutoyo caliper, with 0.01 mm resolution, is used to measure the deformation.

To show how the rapid prototyping system can help manufacture mechanical metamaterials with different acoustic properties, we applied the acoustic technique described above on Sample 1 and Sample 2 samples in compression while obtaining their frequency response between 150 Hz and 1400 Hz at different compression rates. In figure 5 (a) we can observe the transfer function for three states of compression of the sample Sample 1. The yellow star markers represent the response of the metamaterial without compression, with two boundaries fixed to the mechanical press (as shown in Fig.4. Cyan circle markers follow the mechanical response to actuation at 6% compression rate, while blue diamond markers follow the 12% compression rate. The most relevant result showed here is the emergence of an absorption band up to 1000 Hz which moves to higher frequencies for larger compression rates. Figure 5 (b) shows the frequency response of Sample 1 at different deformation levels in a compression-release process. The color map indicates the transfer function amplitude.

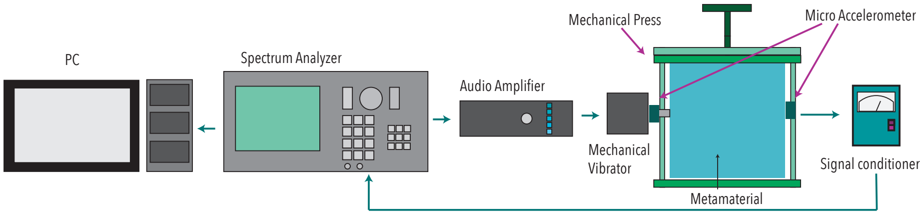

Figure 4. Experimental setup used to obtain power spectrum of mechanical metamaterials under deformation. A spectrum analyzer sends a sweep sine signal, which is amplified by a power audio amplifier. A mechanical vibrator excites the metamaterial and a micro accelerometer receives the response of the metamaterial. The power spectrum is obtained by the spectrum analyzer. The specimen is compressed by a mechanical press and the measurement is repeated.

We can observe an absorption band with constant frequency around 520 Hz, and a second band which appears at 1% compression around 930 Hz which raises up to 1300 Hz at the maximum 12% compression rate, corresponding to a 40% change. The same behavior is observed when we release the sample, which shows the reversibility of the process.

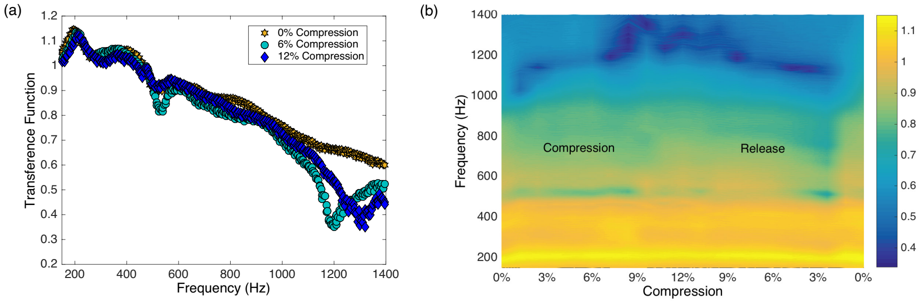

Figure 5. (a) Transfer function for the Sample 1 sample for 0% (★), 6% (●) and 12% (◆) compression rates. (b) Transfer function color map for a mechanical metamaterial sample as a function of frequency and compression rates.

This reversibility can be assessed further when the procedure is repeated. Figure 6 shows the frequency response of Sample 2 in consecutive compression-release ramps. Looking at the first compression zone, we can observe an absorption band around 600 Hz, which appears to split into two bands upon reaching to 2.5% compression rate. The first absorption band appears near 450 Hz, rises around 470 Hz at 3% compression rate and remains constant. The second absorption band rises to 800 Hz at 3% compression rate and remains constant. Finally, a third absorption band is observed up to 1000 Hz. It appears at 2.5% compression rate, around 1060 Hz and reaches a maximum around 1110 Hz at maximum compression. Furthermore, We can confirm the reversibility of this band-gap generation in each compression and release process.

Three relevant aspects of the behavior of these rapidly prototyped mechanical metamaterials was revealed: first, the frequency response is different for mechanical metamaterials with different structures. Secondly, this response depends on the degree of deformation, with absorption bands that can be tuned by compression. Finally, the mechanical tuning of these bands is a reversible process which means that our rapid prototyping method allows the manufacture of tunable elastic mechanical filters.

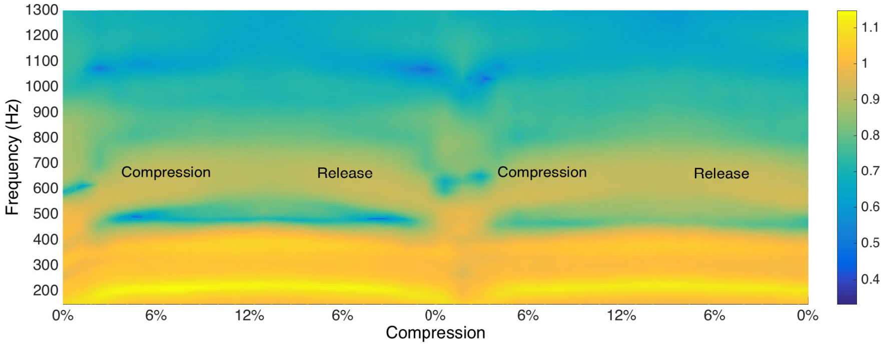

Figure 6. Transfer function color map for the Sample 2 sample as a function of frequency and compression rates in consecutive compression-release ramps.

4. Conclusions

In summary, we have presented a fast, reproducible, simple and accurate method to print soft periodic elastic mechanical metamaterials with tunable band gaps. From an acoustic spectroscopic characterization we have found that the frequency response can be easily tuned by the degree of deformation of the elastic mechanical metamaterial, with absorption bands that can be tuned by compression. We have found that this mechanical response is reversible in a compression-release cycle, opening new oportunities for mechanical and/or acoustic filters with controlled absorption. The encapsulation of droplets can therefore be used to functionalize these novel materials by controlling externally its elastic absorption bands, via mechanical and/or electromagnetic actuation. We envision that this work will impact the materials community as it provides a robust, precise and inexpensive strategy to design and construct architected soft mechanical metamaterials.

5. Acknowledgements

We would like to thank Plataforma Experimental Bio-CT, Faculty of Denstistry from Universidad de Chile (FONDEQUIP EQM150010) for the micro-CT analysis of our samples. We acknowledge the financial support of Fondecyt Grant 1190005, Fondecyt Postdoctorado 3200239, and the Millennium Nucleus ‘Soft Smart Mechanical Metamaterials’ of the Millennium Scientific Initiative of the Ministry of Economy, Development and Tourism (Chile).

1. G. C. Ma, and P. Sheng.“Acoustic metamaterials: From local resonances to broad horizons", *Science Advances*, **2016**, *2* 1501595.
2. K. Bertoldi, V. Vitelli, J. Christensen, and M. van Hecke.“Flexible mechanical metamaterials". *Nature Reviews Materials,* **2017**, *2*, 17066.
3. E. Barchiesi, M. Spagnuolo, and L. Placidi. .“Mechanical metamaterials: a state of the art", *Mathematics and Mechanics of Solids*, **2019**, *24*, 212-234.
4. F. Pan, Y. L. Li, Z. Y. Li, J. L. Yang, B. Liu, and Y. L. Chen, YL. “3D Pixel Mechanical Metamaterials", *Advanced Materials*, **2019**, *31*, 1900548.
5. T. Buckmann, M. Kadic, and M. Wegener.“Mechanical cloak design by direct lattice transformation", *Proceedings of the National Academy of Sciences of the United States of America,* **2015**,*112*, 4930–4934.
6. D. E. Quadrelli, R. Craster, M. Kadic, and F. Braghin, F.“Elastic wave near-cloaking", *Extreme Mechanics Letters,* **2016**, *44*, 101262.

7. Y. H. Xue, and X. Zhang."Self-adaptive acoustic cloak enabled by soft mechanical metamaterials", *Extreme Mechanics Letters,* **2021**, *46*, 101347.
8. A. Shelke, S. Banerjee, A. Habib, E. K. Rahani, R. Ahmed, and T. Kundu."Wave guiding and wave modulation using phononic crystal defects", *Journal of Intelligent Material Systems and Structures,* **2014**, *25*, 1541-1552.
9. M. Miniaci, A. Krushynska, F. Bosia, N. M. Pugno, "Large scale mechanical metamaterials as seismic shields", *New Journal of Physics,* **2016**, *18*, 083041.
10. L. Jin *et al*."Guided transition waves in multistable mechanical metamaterials", *Proceedings of the National Academy of Sciences of the United States of America,* **2020**, *117*, 2319-2325.
11. B. Li, C. Zhang, F. Peng, W. Z. Wang, B. D. Vogt, and K. T. Tan,."Guided transition waves in multistable mechanical metamaterials", *Journal of Materials Chemistry C,* **2021**, *9*, 10.1039/d0tc04999a.
12. H. W. Sun, H. X. Du and P. F. Pai."Theory of Metamaterial Beams for Broadband Vibration Absorption", *Journal of Intelligent Material Systems and Structures,* **2010**, *21*, 1085-1101.
13. H. Peng, and P. F. Pai."Acoustic metamaterial plates for elastic wave absorption and structural vibration suppression", *International Journal of Mechanical Sciences,* **2014**, *89*, 350-361.
14. X. J. Tan *et al*."Real-time tunable negative stiffness mechanical metamaterial", *Extreme Mechanics Letters,* **2020**, *9*, 1100990.
15. I. Gibson, D. W. Rosen and B. Stucker. *Additive Manufacturing Technologies: Rapid prototyping technologies*, 1st ed.; Springer: New York, USA, 2010.
16. B.-J. de Gans, P. C. Duineveld, and U. S. Schubert."Inkjet Printing of Polymers: State of the Art and Future Developments", *Advanced Materials,* **2004**, *16*, 203.
17. R. L. Truby, and J. A. Lewis."Printing soft matter in three dimensions", *Nature,* **2016**, *540*, 371–378.
18. K. Estelle, D. Blair, K. Evans, and B. Arda Gozen. "Manufacturing of smart composites with hyperelastic property gradients and shape memory using fused deposition". *Journal of Manufacturing Processes*, **2017**, *28* 500–507.
19. J. Herzberger, J. M. Sirrine, C. B. Williams, T. E. Long, "Polymer Design for 3D Printing Elastomers: Recent Advances in Structure, Properties, and Printing". *Progress in Polymer Science*, **2019**, *97* 101144.
20. S. Park, W. Shou, L. Makatura, W. Matusik, K. Fu. "3D printing of polymer composites: Materials, processes, and applications". *Matter*, **2022**, *5* 43-76.
21. K. H. Matlack, A. Bauhofer, S. Krodel, A. Palermo, and C. Daraio. "Composite 3D-printed metastructures for low-frequency and broadband vibration absorption". *Proceedings of the National Academy of Sciences of the United States of America,* **2016** *113*, 8386-8390.
22. B. W. Zheng and J. Xu. "Mechanical logic switches based on DNA-inspired acoustic metamaterials with ultrabroad low-frequency band gaps". *Journal of Applied Physics D - Applied Physics,* **2016** *50*, 465601.
23. Y. Y. Chen, G. L. Huang, and C. T. Sun. "Band Gap Control in an Active Elastic Metamaterial With Negative Capacitance Piezoelectric Shunting". *Journal of Vibration and Acoustics - Transaction of the ASME,* **2014** *136*, 061008.
24. S. C. Shan, S. H. Kang, P. Wang, C. Y. Qu, S. Shian, E. R. Chen, and K. Bertoldi. "Harnessing Multiple Folding Mechanisms in Soft Periodic Structures for Tunable Control of Elastic Waves". *Advanced Functional Materials,* **2014**, *24*, 4935-4942.
25. P. Wang, F. Casadei, S. Shan, J. C. Weaver, and K. Bertoldi. "Harnessing Buckling to Design Tunable Locally Resonant Acoustic Metamaterials". *Physical Review Letters,* **2014**, *113*, 014301.
26. A. O. Krushynska, M. Miniaci, F. Bosia, and N. M. Pugno. "Coupling local resonance with Bragg band gaps in single-phase mechanical metamaterials". *Extreme Mechanics Letters,* **2017** *12*, 30-36.
27. Y. F. Wang, Y. Z. Wang, B. Wu, W. Q. Chen, and Y. S. Wang. "Tunable and Active Phononic Crystals and Metamaterials". *Applied Mechanics Reviews,* **2020** *72*, 040801.
28. L. Cai, J. Marthelot, and P. -T. Brun. "An unbounded approach to microfluidics using the Rayleigh-Plateau instability of viscous threads directly drawn in a bath". *Proceedings of the National Academy of Sciences of the United States of America,* **2019** *116*, 22966-22971.
29. L. Cai, J. Marthelot, C. Falcón, P. M. Reis, and P. -T. Brun. "Printing on liquid elastomers". *Soft Matter,* **2020** *16*, 3137-3142.
30. F. Blanc. "Syringe pump to extrude fluids controlled by a 3D printer". https://github.com/blancfer/3dextruder *(2022)*

Annex A.7

Metamaterials with ferrofluid inclusions

The use of ferrofluid as an injection fluid was briefly studied; given its high viscosity, the Rayleigh-Plateau instability for viscous fluids would work to make mechanical metamaterials whose internal structure can be modified over time or with the idea of allowing the transmission of waves in a specific direction.

One reason for this is that by using a fluid that reacts magnetically to make the spherical inclusions, it is possible to structurally perturb the material by placing it in a magnetic field, making it change from a spherical shape to an ellipsoidal shape in the direction in which the field is applied, as shown in Fig.7.3 of the work by Latikka et al. [21], where they study the wetting of ferrofluids, this would allow the transmitted wave to travel in this privileged direction.

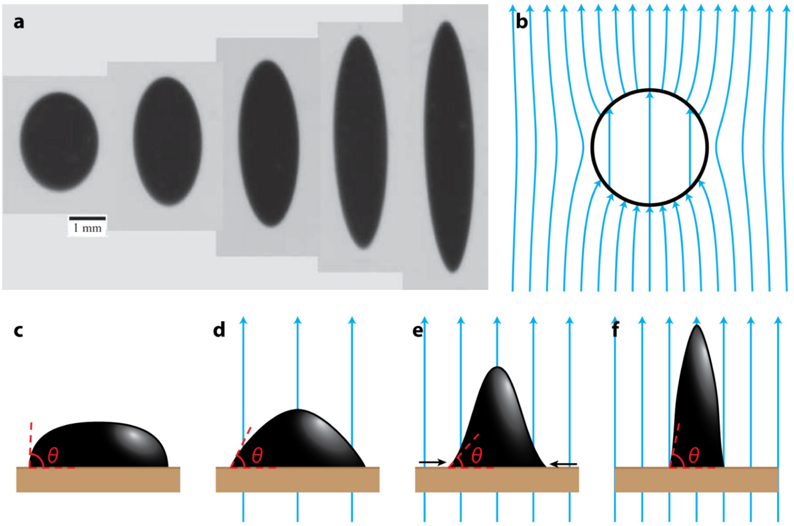

Figure 7.3: Shape of a ferrofluid droplet in an external uniform magnetic field from the work of [21].

The second reason behind this is that with this type of fluid, the process of creating our metamaterials can move from three-dimensional to four-dimensional control by now adding the variable of time in terms of a time-varying magnetic field since doing so will change the behavior of the material as the magnetic field varies.

Experimental attempts were made to see if a drop of fluid was able to sense a magnetic field when encapsulated within the elastic matrix; observations made show that the fluid shows response and can interact with the field when there was a sufficient amount of ferrofluid, the ratio of the amount of fluid to amount of polymer was at least a quarter, or when the field being applied was strong enough, around 500 G.